Chapter 9
Strong Focusing Synchrotron

Abstract This Chapter introduces the strong focusing alternating gradient (AG) and separated function synchrotrons. It provides the theoretical material which the simulation exercises lean on. The chapter begins with a brief reminder of the historical context, and continues with beam optics, chromaticity, acceleration, resonances and resonant extraction, dynamical effects of synchrotron radiation (SR), the electromagnetic SR impulse, and depolarizing resonances. This resorts to basic charged particle optics, acceleration, and dynamics in magnetic fields introduced in the previous Chapters.
The simulation of a strong focusing AG synchrotron requires just two optical elements from `zgoubi` library: DIPOLE or MULTIPOL to simulate a combined function dipole, and DRIFT to simulate straight sections. Main dipoles in a separated function synchrotron can use BEND. It requires in addition quadrupoles, simulated using QUADRUPO or MULTIPOL. The latter can simulate higher order lenses, which can otherwise resort to SEXTUPOL, OCTUPOLE, etc. Acceleration uses CAVITE. Accounting for synchrotron radiation (SR) energy loss requires SRLOSS. Monte Carlo SR monitoring can use SRPRNT, which logs data in zgoubi.res. SRPRNT[PRINT] in addition logs data in zgoubi.SRPRNT.Out. Computation of synchrotron radiation (SR) Poynting and spectral brightness uses `zpop`. Particle monitoring requires keywords introduced in the previous Chapters, including FAISCEAU, FAISTORE, possibly PICKUPS, and some others. Spin motion computation and monitoring resort to SPNTRK, SPNPRT, FAISTORE. Optics matching and optimization use FIT[2]. INCLUDE is used, mostly here in order to simplify the input data files. SYSTEM is used to, mostly, resort to gnuplot so as to end simulations with some specific graphs. Data for the latter are read from output files filled up during the execution of the code, such as zgoubi.fai (resulting from the use of FAISTORE), zgoubi.plt (resulting from IL=2), or other zgoubi.*.out files resulting from a PRINT command. Stepwise particle data logged in zgoubi.plt are used by the interface zpop to compute the electric field impulse of SR and subsequent spectral angular energy density of the radiation.

Notations used in the Text

$\mathbf{B}$; $B_{\mathrm{x,y,s}}$; B	field vector; its components in the moving frame; its modulus
$B\rho = p/q$; $B\rho_0$	particle rigidity; reference rigidity
C; C_0	orbit length; $C = 2\pi R + \left[\begin{smallmatrix}\text{straight}\\ \text{sections}\end{smallmatrix}\right.$; reference, $C_0 = C(p = p_0)$
$\mathbf{E}$; E_σ, E_π	SR electric field impulse; its parallel and normal components
E; E_s	particle energy, $E = \gamma m_0 c^2$; synchronous energy
EFB	Effective Field Boundary
f_{rev}, $f_{\mathrm{rf}} = h\, f_{\mathrm{rev}}$	revolution and RF voltage frequencies
G	gyromagnetic anomaly, $G = 1.792847$ for proton
G; $K = G/B\rho$	quadrupole gradient; focusing strength
h	RF harmonic number
m; m_0; M	particle mass; rest mass; in units of MeV/c^2
$n = -\frac{\rho}{B}\frac{\partial B}{\partial x}$	focusing index
$\mathbf{n}_0$	stable spin precession direction
$\mathbf{P} = \mathbf{E} \times \mathbf{B}$	SR Poynting vector
P_i, P_f	beam polarization, initial, final
$\mathbf{p}$; p; p_0	momentum vector; its modulus; reference
q	particle charge
r; R	orbital radius ; average radius, $R = C/2\pi$
S	periodicity of the lattice; or sextupole strength
s	path variable
U_s	SR energy loss
$\mathbf{v}$; v	particle velocity vector; its modulus
$V(t)$; $\hat{V}$	oscillating voltage; its peak value
x, x', y, y', l, $\frac{dp}{p}$	particle coordinates in the moving frame, $[(*)' = d(*)/ds]$
α	momentum compaction; or trajectory deviation; or depolarizing resonance crossing speed
$\beta = v/c$; β_0; β_{s}	normalized particle velocity; reference; synchronous
β_{u}	betatron functions ($u:\ x, y, Y, Z$)
$\gamma = E/m_0c^2$	Lorentz relativistic factor
γ_{tr}	transition γ, $\gamma_{\mathrm{tr}} = 1/\sqrt{\alpha}$
δp, Δp	momentum offset
ϵ_c	critical energy of SR, $\epsilon_c = \hbar\omega_c = hc/\lambda_c$
ε	wedge angle
ε_u/π	Courant-Snyder invariant; emittance//π ($u:\ x, y, l$)
ϵ_R	strength of a depolarizing resonance
η	phase slip factor, $\eta = \frac{1}{\gamma^2} - \alpha$
μ_{u}	betatron phase advance per period, $\mu_{\mathrm{u}} = \int_{\mathrm{period}} \frac{ds}{\beta_{\mathrm{u}}(s)}$ ($u:\ x, y$)
ν_{u}	wave numbers, horizontal, vertical, synchrotron ($u:\ x, y, l$)
ρ; ρ_0	curvature radius; reference
σ	beam matrix
ϕ; ϕ_{s}	particle phase at voltage gap; synchronous phase
φ_{u}	betatron phase advance, $\varphi_{\mathrm{u}} = \int ds/\beta_{\mathrm{u}}$ ($u:\ x, y, Y, or Z$)
φ	spin angle to the vertical axis
ω_c	critical angular frequency of SR, $\omega_c = 3\gamma^3 c/2\rho$
ω_s; Ω_s	$2\pi f_{\mathrm{rev}}$; synchrotron frequency

9.1 Introduction

In the very manner that the 1930s-1940s cyclotron, betatron, microtron, weak focusing synchrotron, which are still in use today, have since essentially not changed in their concepts and design principles, today the gap profile, yoke and current coil geometry of combined function alternating-gradient (AG) dipoles remain essentially as patented in 1950 (Fig. 9.1) [1].

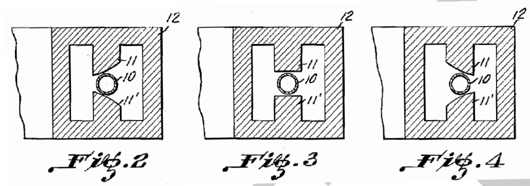

Fig. 9.1 Bending magnet pole profiles for a *focusing system for ions and electrons* [1]. Assuming curvature center to the left, the left (respectively right) profile is defocusing (resp. focusing), the middle profile has zero index

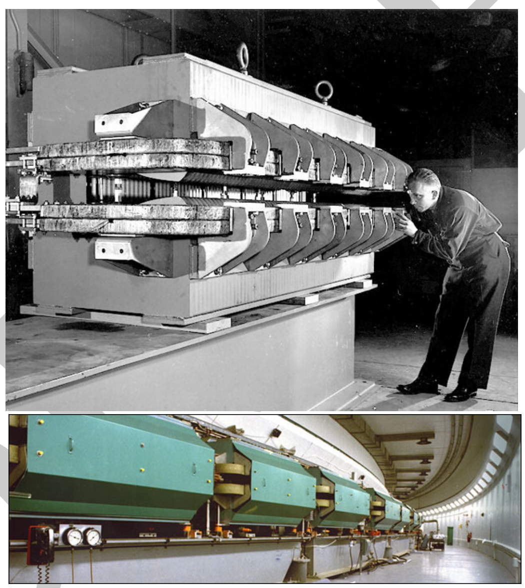

Fig. 9.2 Top: the AGS combined function main dipole. The hyperbolic profile poles are visible, partly hidden by the field coils. Bottom: the 809 m circumference AGS synchrotron, comprised of 240 such dipoles [2]

In 1952, in the context of studies concerning the Cosmotron, strong focusing was devised at the Brookhaven National Laboratory (BNL): *"Strong focusing forces result from the alternation of large positive and negative n-values in successive sectors of the magnetic guide field in a synchrotron. This sequence of alternately* *converging and diverging magnetic lenses* [...] *leads to significant reductions in oscillation amplitude”* [3]. It led to the construction of the first two high-energy AG proton synchrotrons (PS), in the 30 GeV range, in the late 1950s: the CERN PS, and the AGS at BNL (Fig. 9.2). Both remain major pieces, 60 years later, of the respective injection chains of the two largest colliders in operation, the LHC and RHIC. Early works at BNL provided theoretical formalism, still at work today, for the analysis of beam dynamics in synchrotrons [4].

Fig. 9.3 SATURNE 2 strong focusing 3 GeV synchrotron at Saclay [5], successor in the late 1970s of SATURNE 1 weak focusing synchrotron (Fig. 8.1). It was the first strong focusing synchrotron to accelerate polarized ion beams

Fig. 9.4 A quadrupole magnet at LBL in 1957, used for beam lines at the 184-inch cyclotron. An early specimen here, obviously, being a spin-off of the early 1950s concept of strong focusing [6]

Separated function focusing, whereby beam guiding is ensured by uniform field dipoles while focusing is ensured separately by quadrupoles (Fig. 9.3), followed from the development of the latter (Fig.9.4), a spin-off of the strong index technology [7].

The dramatic reduction of transverse beam size by strong focusing allows guiding and focusing magnets with small aperture, from lowest energies: medical synchrotrons in the 100 MeV range for instance, to highest ones: hundreds of GeV to multi-TeV range particle physics and nuclear physics colliders (Fig. 9.5). Beams in all these machines are essentially confined in a sub-centimeter or sub-millimeter scale transverse space. A synchrotron is a string of dipole and multipole magnets through which runs a vacuum pipe of a few centimeters diameter (hadron rings) or a few millimeters (electrons). The size of the ring is essentially determined by its circumference, proportional to the magnetic rigidity. This revolutionized the race to high energies, from the prior few GeV weak focusing synchrotrons and their huge magnets, to todays 7 TeV, 27 km long LHC and with further plans for 100 TeV, 100 km circumference colliders [8]. Strong focusing fostered the development of high energy synchrotron light sources around the world, with high brightness synchrotron radiation (SR) from UV to gamma rays produced in electron storage rings in up to multi-GeV energy range.

Fig. 9.5 In RHIC tunnel at the Brookhaven National Laboratory [2]. The two rings of the 255 GeV polarized proton beams and heavy ion collider run parallel over 3.8 km, and intersect at two experiments, STAR and SPHENIX

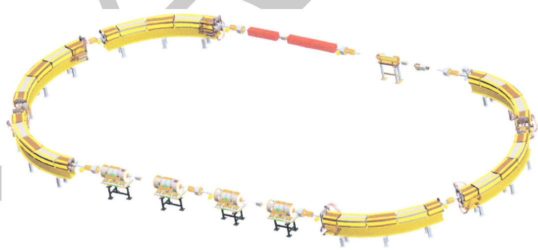

Fig. 9.6 The ion rapid cycling medical synchrotron (iR-CMS) [9], an ion beam RCS for the treatment of cancer tumors

AG focusing is still resorted to today, for instance in the hadrontherapy application (Fig. 9.6), light source lattice [10], and other high energy collider design [11], as it has the merit of compactness. On the other hand, the flexibility of separated function optics made it more popular: it allows to introduce modular functions in complex ring designs such as dispersion suppression sections, low-beta or insertion device sections, long straights, et cetera. Low-emittance, high-brightness light source lattices have complicated focusing further, by introducing longitudinal field gradient bending systems to minimize equilibrium beam emittance [12].

Due to the necessary ramping of the field in order to maintain a constant orbit, synchrotron accelerators are pulsed, storage rings in some cases as well, high energy colliders in particular to bring beams to highest store energy. The acceleration is cycled and the accelerating voltage frequency as well in ion accelerators, from injection to top energy. If the ramping uses a constant electromotive force, then (Eq. 8.3)

$$B(t) \approx \frac{t}{\tau} \tag{9.1}$$

$\dot{B} = dB/dt$ does not exceed a few Tesla/second, thus the repetition rate of the acceleration cycle if of the order of a Hertz. If instead the magnet winding is part of a resonant circuit then the field oscillates,

$$B(t) = B_0 + \frac{\hat{B}}{2}(1 - \cos\omega t) \tag{9.2}$$

so that, in the interval of half a voltage repetition period (*i.e.*, $t : 0 \to \pi/\omega$) the field increases from an injection threshold value to a maximum value at highest rigidity, $B(t) : B_0 \to B_0 + \hat{B}$. The latter determines the highest achievable energy: $\hat{E} = pc/\beta = q\hat{B}\rho c/\beta$. The repetition rate with resonant magnet cycling can reach a few tens of Hertz, a technique known as a rapid-cycling synchrotron (RCS). In both cases anyway B imposes its law and other parameters, comprising the acceleration cycle, the RF frequency in particular, will follow B(t).

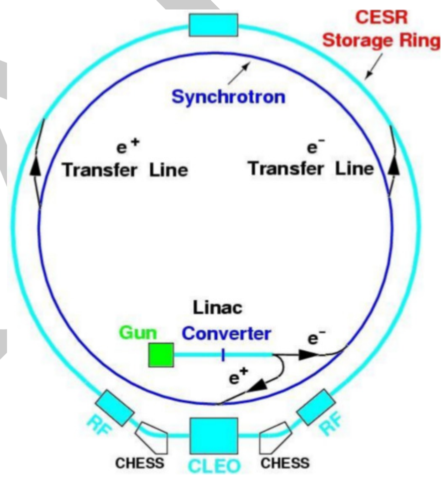

Fig. 9.7 Cornell rapid cycling synchrotron, 5 GeV injector of CESR storage ring [13]

Instances of RCS rings include Cornell 12 GeV, 60 Hz electron AG synchrotron [14] (Fig. 9.7), commissioned in 1967 with a 7 GeV beam, a world record at the time, and still in operation half a century later as the injector of Cornell 5 GeV storage ring (CESR/CHESS) [15]; Fermilab 8 GeV, 60 Hz Booster, which provides protons for the production of neutrino beams; the 30 GeV 500 kW proton beam J-PARC facility in Japan. Rapid cycling is also considered in ion-therapy applications (Fig. 9.6).

To conclude on these preliminaries, lets mention the giants among accelerator facilities which nuclear (NP) and particle (HEP) physics research laboratories are: so far, strong focusing synchrotrons happen to be the building blocks from which

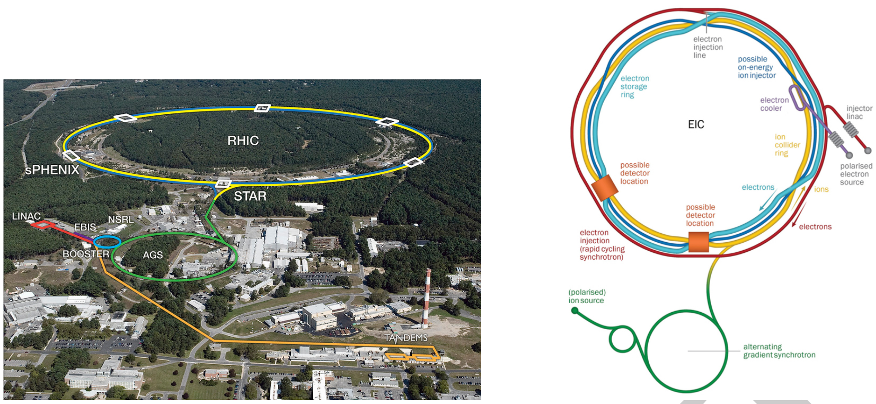

Fig. 9.8 RHIC complex at the Brookhaven National Laboratory (left) [2], a cascade of 4 strong focusing ion synchrotrons: the AGS and its Booster, and the 3.8 km circumference intersecting RHIC rings, in motion towards the EIC project (right) [16] which will add 2 electron synchrotrons: an 18 GeV storage ring and its RCS injector

they are constructed. This is so at the CERN LHC complex. This is apparent also in Fig. 9.8 which shows RHIC heavy ion collider complex, and its planned evolution, the Electron-Ion Collider [17][1] The next colliders could be linacs, it was at SLAC with the SLC [18], it was the plan with such projects as TESLA [19], the NLC [20]. The interest of NP and HEP will decide on the research tools: more large synchrotron rings for a muon collider [21], an FCC-ee, -hh and other -eh [8], or high gradient linacs for the ILC [22]. or for ReLic e^+e^- collider [23]. Or new acceleration methods and technologies?

9.2 Basic Concepts and Formulæ

Alternating gradient focusing is sketched in Fig. 9.9. An order of magnitude of

Fig. 9.9 Horizontally focusing lenses (field index $n \gg 0$, the solid red trajectory) are vertically defocusing ($n \ll 0$, the dashed blue trajectory), and vice versa. This imposes alternating gradients in order for a sequence to be globally focusing, for both planes

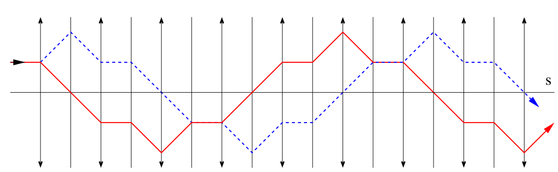

[1] Beam polarization studies have been using `zgoubi` in all five EIC synchrotrons.

the focusing index can be estimated from the fields met in these structures: say a maximum B$\sim$1 Tesla in the dipole gap, same at pole tip in quadrupoles $\sim$10 cm off axis. The latter results in $\frac{\Delta B}{\Delta x} \sim 10$ T/m, the former in meters to tens of meters dipole curvature radius. All in all, in absolute value,

$$n = -\frac{\rho}{B}\frac{\partial B}{\partial x} \sim \frac{10^{0\sim 2}_{[\mathrm{m}]}}{1_{[\mathrm{T}]}} \times 10_{[\mathrm{T/m}]} \sim 10^{1\sim 3} \quad \gg 1 \tag{9.3}$$

much greater than in a weak focusing structure, characterized by $0 < n < 1$.

9.2.1 Components of the Strong Focusing Optics

Combined function (AG) optics

This is, typically, the BNL AGS and CERN PS optics, using dipoles that ensure both beam guiding and focusing (Fig. 9.2). Separate quadrupole and multipole lenses have later been introduced as they provide knobs for the adjustment of optical functions and other parameters. AG optics is still topical in modern designs, as in the iRCMS whose six 60 deg arcs are comprised of a sequence of five focusing and defocusing combined function dipoles [9], Fig. 9.6.

Field

Referring to normal conducting magnet technology, a hyperbolic pole profile (Fig. 9.1) is an equipotential (a line of constant scalar potential V) of equation

$$V_{\mathrm{pole}} = A\,xy$$

at the origin of a magnetic field $\mathbf{B} = \mathbf{grad}\,V$, everywhere perpendicular to the equipotential. A combined function dipole with mid-plane geometrical symmetry is defined by materializing two equipotentials, at $\pm V_{\mathrm{pole}}$ (Fig. 9.10). This results in a

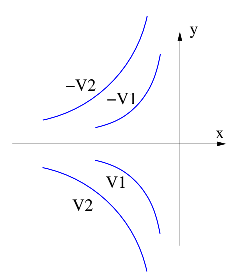

Fig. 9.10 Symmetric materialization of pole profiles, at $\pm V$. Nothing would preclude materializing poles at V_1 and $-V_2$ potentials, with the same resulting field between the poles

vertical field component $B_y = \partial V/\partial y = Ax$, and therefore a radial field index

$$n = -\frac{\rho}{B_y}\frac{\partial B_y}{\partial x}\bigg|_{y=0} = \frac{\rho}{B_y}A$$

A is a constant, typically up to $\sim$ 10 T/m, *cf.* Eq. 9.3. The pole profile opens up either inward (toward the center of curvature, a horizontally focusing dipole, vertically defocusing) or outward (a vertically focusing dipole, horizontally defocusing), Fig. 9.11.

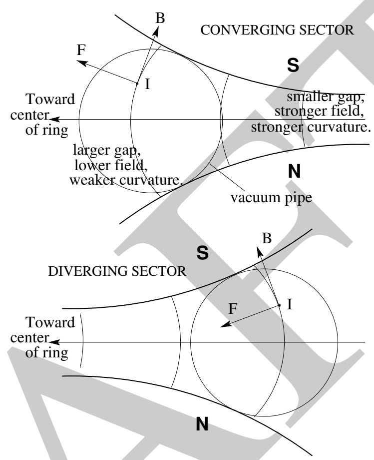

Fig. 9.11 Beam focusing in combined function dipoles. The center of curvature is to the left. The pole profile follows an equipotential $V = Axy$. Top: the pole profile opens up towards the center of curvature → the dipole is horizontally converging (vertically diverging: current I comes out of the page, force **F** results from field **B**). Bottom: pole profile closing toward the center of curvature → the dipole is horizontally diverging, vertically converging

In a bent AG dipole a line of constant field is an arc of a circle; the field guides the reference particle along the arc in the median plane. The mid-plane field can be expressed under the form

$$B_y(r,\theta) = \mathcal{G}(r,\theta)\, B_0 \left(1 + n\,\frac{r-r_0}{r_0} + n'\left(\frac{r-r_0}{r_0}\right)^2 + n''\left(\frac{r-r_0}{r_0}\right)^3 + \ ...\right) \quad (9.4)$$

with r_0 the reference (normally the orbit) radius. Higher order indices, sextupole n', octupole n'', ..., may be residual effects from fabrication tolerances, magnetic saturation, deformation of yoke with years, etc., or included by design, with significant value.

In a straight AG dipole, a line of constant field is a straight line; an instance is the AGS main magnet (Fig. 9.2). Another instance is the Fermilab recycler arcs permanent magnet dipole, which includes quadrupole and sextupole components [24, 25]. The modeling of the field in a straight combined function dipole can be derived from the scalar potential of Eq. 9.5.

Separated function optics

In a separated function lattice quadrupole lenses ensure the essential of the focusing, main bends have zero index. In smaller rings though, geometrical focusing in bending magnets may be significant (Sect. 8.2.1.2, Fig. 8.6). Wedge angles in addition may be introduced and contribute horizontal and vertical focusing/defocusing (Fig. 8.8).

Higher order multipole lenses are used for the compensation of adverse effects: coupling, aberrations, space charge, impedance, etc., and for beam manipulations: controlling the coupling, resonant extraction, etc.

The field in a multipole of order n ($n = 1, 2, 3$, etc.: dipole, quadrupole, sextupole, etc.) derives, via $\mathbf{B} = \mathbf{grad}V$, from the Laplace potential [26]

$$V_n = (n!)^2 \left\{ \sum_{\mathrm{q}=0}^{\infty} (-)^q \alpha_{\mathrm{n},0}^{(2q)}(s) \frac{(x^2+y^2)^q}{4^q q!(n+q)!} \right\} \left\{ \sum_{m=0}^{n} \frac{x^{n-m} y^m}{m!(n-m)!} \sin m\frac{\pi}{2} \right\} \tag{9.5}$$

where $\alpha_{\mathrm{n},0}^{(2q)}(s) = d^{2q}\alpha_{\mathrm{n},0}(s)/ds^{2q}$ accounts for the s-dependence of the potential. Technologies for multipoles and combined multipoles include pole profiling, permanent magnets [24, 27], superconducting $\cos n\theta$ winding as in RHIC and LHC colliders, and variants.

In a hard-edge field model the $\sum_{\mathrm{q}=0}^{\infty}$ series is reduced to the $q = 0$ term, with the following outcomes [28, 29].

Quadrupole

The equipotential (the pole profile) is an equilateral hyperbola, of equation Gxy =constant in an upright quadrupole (left figure below), and $G(x^2 - y^2)$ =constant in a $\pi/4$ skew quadrupole (right). The resulting field writes

$$B_x = \frac{\partial V}{\partial x} = Gy \qquad B_y = \frac{\partial V}{\partial y} = Gx$$

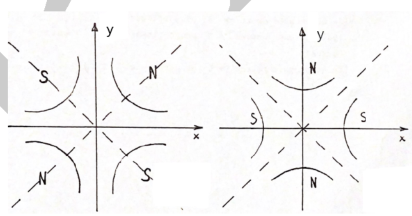

$$B_x = Gx \qquad B_y = -Gy$$

Upright quadrupoles are used for focusing, skew quadrupoles are used to compensate, or introduce, transverse coupling. The focusing strength

$$K = \frac{1}{L}\frac{\int G(s)\,ds}{p/q} \tag{9.6}$$

is momentum-dependent.

Sextupole

The equipotential satisfies $H(3x^2y - y^3)$ =constant in an upright sextupole (left), $H(x^3 - 3xy^2)$ =constant in a $\pi/6$ skew sextupole (right), with resulting field

$$B_x = 2Hxy \qquad B_y = H(x^2 - y^2)$$

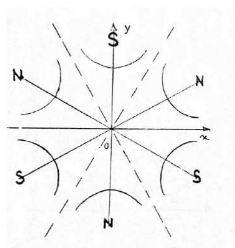

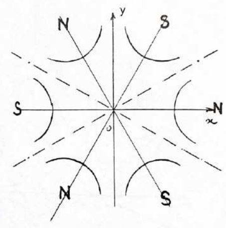

$$B_x = H(x^2 - y^2) \qquad B_y = -2Hxy$$

Upright sextupoles introduce a vertical field component $B_y \propto x^2$, they are used to correct optical aberrations, to modify the momentum dependence of the wave numbers ν_x, ν_y, and in beam manipulations such as resonant extraction. Skew sextupoles introduce a radial field component $B_x \propto y^2$, they are used to correct optical aberrations.

Octupole

The equipotential pole profile satisfies $O(x^3y - xy^3)$ =constant in an upright octupole (left), $O(x^4 - 6x^2y^2 + y^4)$ =constant in a $\pi/8$ skew octupole (right), yielding the field

$$B_x = O(3x^2y - y^3) \qquad B_y = O(x^3 - 3xy^2)$$

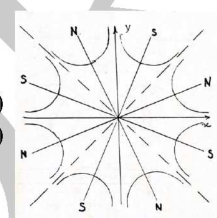

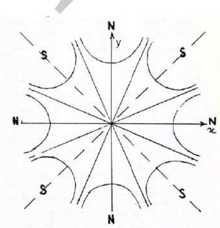

$$B_x = O(x^3 - 3xy^2) \qquad B_y = -O(3x^2y - y^3)$$

Upright octupoles are used to introduce a vertical field component $B_y \propto x^3$; skew octupoles introduce a vertical field component $B_y \propto y^3$. Octupoles are used to correct aberrations, or to modify the amplitude dependence of wave numbers.

9.2.2 Transverse Motion

The transverse motion of a particle in the S-periodic lattice of a cyclic accelerator, at design momentum p_0 and with curvature radius ρ_0, satisfies Hill's equations[2]

$$\frac{d^2x}{ds^2} + K_x(s)x = \frac{1}{\rho_0}\frac{\Delta p}{p_0}, \qquad \frac{d^2y}{ds^2} + K_y(s)y = 0 \tag{9.7}$$

where $K_x(s)$, $K_y(s)$ have the periodicity of the lattice ($K_{\substack{x\\y}}(s+S) = K_{\substack{x\\y}}(s)$), and depend locally on the nature of the optical elements, in the following way.

Case of

$$-\text{ dipole}: \begin{cases} K_x = \dfrac{1-n}{\rho_0^2} \\ K_y = \dfrac{n}{\rho_0^2} \end{cases} \qquad \left(n = -\frac{\rho_0}{B_0}\frac{\partial B_y}{\partial x}\right) \tag{9.8}$$

$$-\text{ a wedge at } \mathrm{s} = \mathrm{s_w}: \left\{ K_{\substack{x\\y}} = \pm\frac{\tan\varepsilon}{\rho_0}\delta(s - s_w) \right. \qquad \left(\text{with } \varepsilon \lesseqgtr 0 \text{ if } \begin{matrix}\text{focusing}\\ \text{defocusing}\end{matrix}\right)$$

$$-\text{ quadrupole}: K_{\substack{x\\y}} = \frac{\pm \mathrm{G}}{B\rho};\ \frac{1}{\rho_0} = 0 \qquad \left(\text{gradient } G = \frac{\text{field at pole tip}}{\text{radius at pole tip}}\right)$$

$$-\text{ drift space}: K_x = K_y = 0;\ \frac{1}{\rho_0} = 0$$

By contrast with the betatron and weak focusing technologies, strong focusing with its independent focusing ($G > 0$) and defocusing ($G < 0$) gradient families allows separate adjustment of the horizontal and vertical focusing strengths, and wave numbers as a consequence.

The on-momentum ($p = p_0$) closed orbit coincides with the reference axis of the optical elements. The betatron motion for an on-momentum particle satisfies Eq. 9.7 with $\Delta p = 0$. Solving the latter (see Sect. 8.2.1.3) requires introducing two independent solutions $u_{\substack{1\\2}}(s)$ (Eq. 8.12), the linear combination of which yields the pseudo harmonic motion (Eq. 8.14)

$$\left| \begin{aligned} & u(s) = \sqrt{\beta_u(s)\varepsilon_u/\pi}\, \cos\left(\int \frac{ds}{\beta_u(s)} + \varphi_u\right) \\ & u'(s) = -\sqrt{\frac{\varepsilon_u/\pi}{\beta_u(s)}}\, \sin\left(\int \frac{ds}{\beta_u(s)} + \varphi_u\right) + \alpha(s)\, \cos\left(\int \frac{ds}{\beta_u(s)} + \varphi_u\right) \end{aligned} \right. \tag{9.9}$$

The motion satisfies the Courant-Snyder invariant, namely (Fig. 9.12)

---

[2] Acceleration, or deceleration, adds a velocity term, betatron damping results. This is addressed in "Betatron damping", Sect. 10.2.3, where it accounts in addition for a non-constant varying orbital radius.

$$\gamma_u(s)u^2 + 2\alpha_u(s)uu' + \beta_u(s)u'^2 = \frac{\varepsilon_u}{\pi} \tag{9.10}$$

i.e., the surface of the phase space ellipse is a constant of the motion. Its form and orientation (Fig. 9.12) change along the period as a consequence of the strong modulation of the betatron functions (Fig. 9.13), far more than in a weak focusing lattice which features weak betatron modulation: $\alpha_u(s) \approx 0$ and $\beta_u(s) \approx$constant (Figs. 8.9, 8.10).

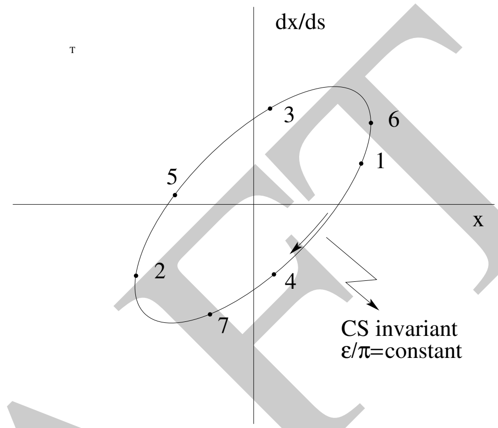

Fig. 9.12 Courant-Snyder invariant and turn-by-turn harmonic motion along the invariant, observed at some azimuth s. The aspect ratio of the ellipse depends on the observation azimuth s but its area ε_u is invariant

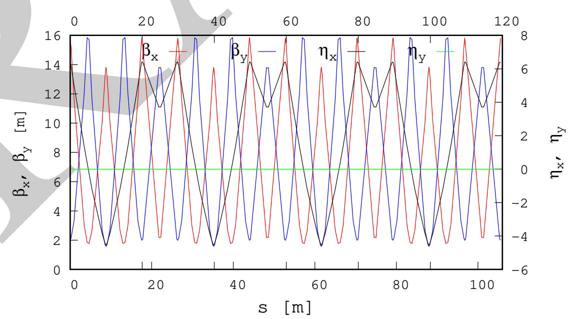

Fig. 9.13 Optical functions around SATURNE 2 synchrotron, a 4-period FODO cell lattice

Beam envelopes are given by the extrema,

$$\hat{x}_{\text{env}}(s) = \pm\sqrt{\beta_x(s)\frac{\varepsilon_x}{\pi}}, \qquad \hat{y}_{\text{env}}(s) = \pm\sqrt{\beta_y(s)\frac{\varepsilon_y}{\pi}} \tag{9.11}$$

Phase space motion

Write the two independent solutions $u_{\frac{1}{2}}(s)$ (Eq. 8.12) under the form

$$u_1(s) = \underbrace{F(s)}_{\text{S-periodic}} \times \underbrace{e^{i\mu\frac{s}{S}}}_{\frac{2\pi S}{\mu}\text{-periodic}} \quad \text{and} \quad u_2(s) = u_1^*(s) = F^*(s)\, e^{-i\mu\frac{s}{S}} \tag{9.12}$$

where

$$F(s) = \sqrt{\beta_u(s)}\, e^{i\left(\int_0^s \frac{ds}{\beta_u(s)} - \mu\frac{s}{S}\right)} \tag{9.13}$$

Introduce

$$\psi_u(s) = \int_0^s \frac{ds}{\beta_u(s)} - \mu\frac{s}{S} \tag{9.14}$$

so that $F(s) = \sqrt{\beta_u(s)}\, e^{i\psi_u(s)}$. Equation 9.9 thus takes the form

$$\left|\begin{aligned} u(s) &= \overbrace{\sqrt{\beta_u(s)\varepsilon_u/\pi}}^{S\text{-periodic}}\ \overbrace{\cos\left[\nu\frac{s}{R} + \underbrace{\psi_u(s)}_{\text{S-per.}} + \varphi_u\right]}^{\frac{2\pi S}{\mu}\text{-periodic}} \\ u'(s) &= -\sqrt{\frac{\varepsilon_u/\pi}{\beta_u(s)}}\ \sin\left[\nu\frac{s}{R} + \psi_u(s) + \varphi_u\right] + \alpha(s)\cos\left[\nu\frac{s}{R} + \psi_u(s) + \varphi_u\right] \end{aligned}\right. \tag{9.15}$$

where $\nu = \frac{N\mu}{2\pi}$. Thus, as the betatron function $\beta_u(s)$ and phase $\psi_u(s)$ are S-periodic, the turn-by-turn motion observed at a given azimuth s (*i.e.*, $u(s)$, $u(s+S)$, $u(s+2S)$, ...) is sinusoidal and its frequency is $\nu = N\mu/2\pi$. Successive particle positions $(u(s), u'(s))$ in phase space lie on the Courant-Snyder invariant (Eq. 9.10). The working point (ν_x, ν_y) fully characterizes the first order optical setting of the lattice.

Off-momentum motion

The motion of an off-momentum particle satisfies the inhomogeneous Hill's horizontal differential Eq. 9.7. The chromatic closed orbit

$$x_{\text{ch}}(s) = D_x(s)\frac{\delta p}{p} \tag{9.16}$$

is a particular solution of the equation, its periodicity is that of the cell.

By contrast with a weak focusing lattice where chromatic closed orbits are parallel (Eq. 8.26), in a strong focusing lattice they are distorted (Fig. 9.13), their excursion depends on the distribution along the cell of (i) the dispersive elements which are the dipoles, and (ii) the focusing.

The horizontal motion of an off-momentum particle is a superposition of the particular solution (Eq. 9.16) and of the betatron motion, solution of the homogeneous Hill's equation (Eq. 9.15), namely

$$x(s) = x_\beta(s) + x_{\mathrm{ch}}(s) = \sqrt{\beta_x(s)\frac{\varepsilon_x}{\pi}}\,\cos\left(\int \frac{ds}{\beta_x} + \varphi_x\right) + D_x(s)\frac{\delta p}{p_0} \tag{9.17}$$

whereas the vertical motion is unchanged (Eq. 9.15 taken for $u(s) \equiv y(s)$).

Chromaticity

The focusing strength of combined function dipoles and quadrupoles is a decreasing function of particle rigidity $B\rho = p/q$ (Eq. 9.8). In a ring this affects the horizontal and vertical wave numbers, an effect quantified as the chromaticity, $\xi_{\mathrm{x,y}}$. To the first order in $\delta p/p$, this writes

$$\delta\nu_{\mathrm{x,y}} = \xi_{\mathrm{x,y}}\,\frac{\delta p}{p} \tag{9.18}$$

A linear lattice has a natural chromaticity. Over a distance $\mathcal{L}$ it is given by

$$\xi_{\mathrm{x,y}} = \frac{-1}{4\pi}\int_{\mathcal{L}} \beta_{\mathrm{x,y}}(s)K_{\mathrm{x,y}}(s)ds \tag{9.19}$$

Use a circular integral, $\oint$ in the case of a ring. The natural chromaticity is a negative quantity: focusing decreases with increasing momentum.

One consequence of the chromaticity is that beam momentum spread $\delta p/p$ results in a tune spread $\delta\nu_{\mathrm{x,y}} = \xi_{\mathrm{x,y}} \times \delta p/p$, a beam occupies an extended area in the tune diagram. For this reason in particular, the chromaticity is usually corrected. This is realized by placing sextupoles in dispersive sections, at least two families: a family of horizontal lenses (strength H_x) located at large β_x and a family of vertical lenses (strength H_y) located at large β_y.

The effect leaned on is the following:

- betatron motion $x_\beta(s)$ of particles with momentum $p_0 + \Delta p$ is around an off-centered, chromatic closed orbit $x_{\mathrm{ch}}(s)$ (Eq. 9.16);

- introducing a sextupole results in a local gradient as $B_y \propto (x_{\mathrm{ch}} + x_\beta)^2 = x_{\mathrm{ch}}^2 + 2x_{\mathrm{ch}}x_\beta + x_\beta^2$, namely, $\left.\frac{\partial B_y}{\partial x}\right|_{x=x_{\mathrm{ch}}} = 2x_{\mathrm{ch}} = 2D_x\frac{\Delta p}{p}$. This results in a focusing force proportional to $\delta p/p$. Sextupoles contribute to chromaticity (or its compensation) following

$$\xi_{\mathrm{x,y}} = \frac{1}{4\pi}\int H_{\mathrm{x,y}}(s)\beta_{\mathrm{x,y}}(s)D_x(s)ds \tag{9.20}$$

9.2.3 Resonances

Consider the excitation of transverse beam motion by a generator of frequency Ω located at some azimuth along the ring [29]. The action of the excitation $S \times \sin \Omega t$ on the oscillating motion $u(t)$ can be written under the form

$$\frac{d^2u}{dt^2} + \omega^2 u = S \sin \Omega t \tag{9.21}$$

Assume harmonic motion for simplicity (as in a weak focusing lattice). Take generator amplitude S =constant, the solution (superposition of the solution of the homogeneous differential equation and of a particular solution of the inhomogeneous differential equation) writes

$$u(t) = U \cos(\omega t + \varphi_u) + \frac{S}{\omega^2 - \Omega^2} \sin \Omega t \tag{9.22}$$

If betatron motion and excitation are in synchronism, *i.e.* on the resonance, $\omega = \Omega$, a particular solution of Eq. 9.21 is

$$u_r(t) = -\frac{S\,t}{2\Omega} \cos \Omega t$$

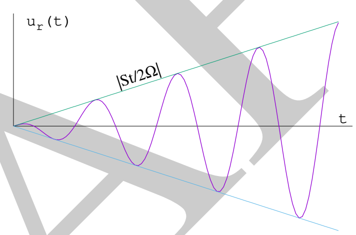

the amplitude of the oscillatory motion grows rapidly with time, at a rate $|St/2\Omega|$.

Assume the amplitude S to be T'-periodic instead, angular frequency $\omega' = 2\pi/T'$, take its Fourier expansion

$$S(t) = \sum_{p=0}^{\infty} a_p \cos(p\omega' t + \varphi_p)$$

the equation of motion thus writes

$$\begin{aligned} &\frac{d^2u}{dt^2} + \omega^2 u = \textstyle\sum_{p=0}^{\infty} a_p \cos(p\omega' t + \varphi_p)\ \sin \Omega t = \\ &\textstyle\sum_{p=0}^{\infty} \frac{a_p}{2} \Big[\sin[(\Omega - p\omega')t + \varphi_p] + \sin[(\Omega + p\omega')t + \varphi_p] \Big] \end{aligned} \tag{9.23}$$

Resonance may occur at generator frequencies $\Omega = \omega \pm p\omega'$, the strength depends on the amplitude a_p of the excitation harmonics. A generator at some point in the lattice excites all harmonics with equal amplitudes a_p. In the case of an extended excitation source, low harmonics only matter.

Sextupole and octupole resonances

The horizontal motion in the presence of sextupoles ($B_y(\theta)|_{\mathrm{y=0}} = S(\theta)x^2$) satisfies

$$\frac{d^2x}{d\theta^2} + \nu_x^2 x = S(\theta)x^2 \tag{9.24}$$

Assume weak perturbation of the motion, so that $x(\theta) \approx \hat{x}\cos(\nu_x\theta+\varphi_x)$, the solution for unperturbed motion. Assume also $S(\theta)$ 2π-periodic. Substitute its Fourier series expansion $S(\theta) = \sum_{p=0}^{\infty} a_p \cos(p\theta + \varphi_p)$ in Eq. 9.24, develop to get

$$\begin{aligned} &\frac{d^2x}{d\theta^2} + \nu_x^2 x = \frac{\hat{x}^2}{2}\Big[\textstyle\sum_{\mathrm{p=0}}^{\infty} a_p \cos(p\theta + \varphi_p) \ + \\ &\tfrac{1}{2}\textstyle\sum_{\mathrm{p=0}}^{\infty} a_p \left[\cos[(p-2\nu_x)\theta + \varphi_p - 2\varphi_x] \ + \ \cos[(p+2\nu_x)\theta + \varphi_p + 2\varphi_x]\right]\Big] \end{aligned} \tag{9.25}$$

Thus resonance may occur at the betatron frequency families $\nu_x = \pm p$, $\nu_x = \pm(p - 2\nu_x)$, and $\nu_x = \pm(p + 2\nu_x)$, *i.e.*,

$$\left[\begin{array}{l} \nu_x = \mathrm{p} \\ 3\nu_x = \mathrm{p} \end{array}\right.$$

In the case of a single sextupole in the ring, all the harmonics p are excited with the same amplitude a_p.

An octupole introduces a field component $B_y(\theta)|_{\mathrm{y=0}} = O(\theta)x^3$. A similar development yields

$$\left[\begin{array}{l} \nu_x = \mathrm{p} \\ 2\nu_x = \mathrm{p} \\ 4\nu_x = \mathrm{p} \end{array}\right.$$

Resonances in a general manner occur at betatron frequencies satisfying

$$m\nu_x + n\nu_y = \text{integer}$$

In this coupling regime one has

$$\frac{\varepsilon_x}{m} - \frac{\varepsilon_y}{n} = \text{constant}, \qquad \text{an invariant of the motion} \tag{9.26}$$

From this it results that,

- if m and n have opposite signs the resonance causes energy exchange between the horizontal and vertical motions: $\frac{\varepsilon_x}{|m|} + \frac{\varepsilon_y}{|n|}$ = constant, an increase of ε_x correlates with a decrease of ε_y and vice-versa. In the presence of linear coupling for instance, $\nu_x - \nu_y$ = integer, $\varepsilon_x + \varepsilon_y$ = constant. An increase in motion amplitude anyway may cause particle loss, an issue in cyclotrons where the Walkinshaw resonance $\nu_x = 2\nu_y$ causes vertical beam loss due to the increase of ε_y;

- if m and n have the same sign the resonance is liable to induce motion instability: $\frac{\varepsilon_x}{m} - \frac{\varepsilon_y}{n}$ = constant, ε_x and ε_y may both increase with no limit.

Resonant Extraction

Resonant extraction is based on the effect of a non-linear force on a dynamical system. A linear regime, under the effect of linear forces, satisfies Eq. 9.7. If $x(s)$ is a stable solution, so is $\lambda x(s)$ (λ a proportionality constant). Introducing a non-linear force modifies the equation of motion, into for instance

◇ $\dfrac{d^2x}{ds^2} + K_x(s)x = S(s)x^2$: sextupole perturbation,

◇ $\dfrac{d^2x}{ds^2} + K_x(s)x = O(s)x^3$: octupole perturbation,

If $x(s)$ is a stable solution, it may no longer be the case for $\lambda x(s)$. If $x(s)$ is small enough the motion, subject to linear and non-linear forces, is quasi-linear and stable. However, increasing the motion amplitude will at some point result in unstable motion. In the (x, x') phase space, the stable regime is bounded by a separatrix. Outside the latter the motion is essentially unstable, or liable to reach amplitudes beyond transverse acceptance of the accelerator (Fig. 9.14).

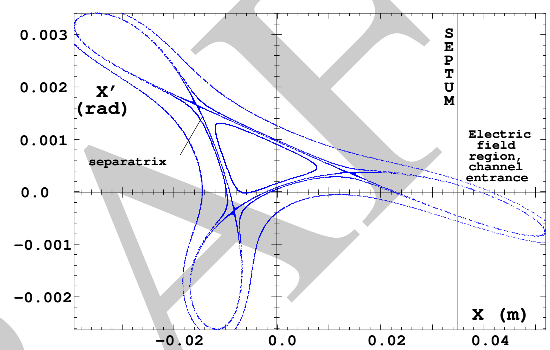

Fig. 9.14 Horizontal motion near a 3rd integer resonance. Within the triangle separatrix the motion is stable. Outside the triangle, motion reaches large amplitudes. An electrostatic septum extracts particles which jump to the right of the septum (into the extraction channel) during their motion

9.2.4 Acceleration. Synchrotron Motion

Particle motion in longitudinal phase space (phase, momentum) and its stability are determined by the lattice and by the acceleration parameters, as introduced in Sect. 8.2.2. They include the

- RF $f_{\mathrm{rf}} = h f_{\mathrm{rev}}$,
- voltage $V(t) = \hat{V} \sin \int \omega_{\mathrm{rf}} dt$,
- synchronous phase ϕ_s (phase of the particle in synchronism with the RF oscillation), which increases by $2\pi h$ per turn,
- transition $\gamma_{\mathrm{tr}} = 1/\sqrt{\alpha}$ (Fig. 8.15).

In the case of weakly modulated betatron functions (weak focusing lattice; AG lattice to some extent), $\alpha \approx 1/\nu_x^2$ so that

$$\gamma_{tr} \approx \nu_x$$

This is the case of SATURNE 1: a weak focusing lattice (see Chap. 8 and simulation exercises there) operated above transition as $\gamma_{tr} = \nu_x \approx 0.6$. In the AGS at BNL the working point is $\nu_x \approx 8.7$ whereas $\gamma_{tr} = 8.4 \approx \nu_x$; transition is crossed as proton beams are accelerated from $\gamma \approx 3$ to $\gamma \approx 25$. Instead, SATURNE 2 strong focusing lattice was operated at negative α, $\eta = \frac{1}{\gamma^2} - \alpha$ does not cancel, γ_{tr} is pure imaginary.

The energy gain per turn at the cavity is

$$\Delta W = 2\pi R\, q\rho \dot{B} = q\hat{V} \sin\phi_s$$

ΔW is imposed by the field law in order to ensure that at all time the synchronous particle momentum satisfies

$$p_s(t) = qB(t)\rho$$

Phase stability

Particles with phase and momentum offsets $(\Delta\phi, \Delta p/p_s) = (\phi - \phi_s, (p - p_s)/p_s)$ in the vicinity of the synchronous particle at (ϕ_s, p_s) undergo periodic longitudinal oscillations. The longitudinal motion satisfies the differential equations

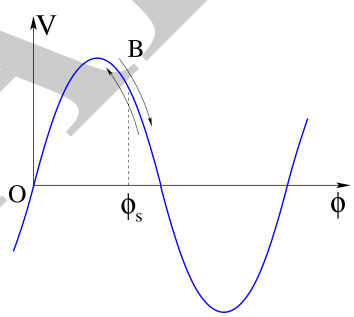

Fig. 9.15 In the presence of RF, particles oscillate in the vicinity of the synchronous phase. Above transition, in this schematic

$$\frac{d\Delta\phi}{dt} = h\eta\omega_s \frac{\Delta p}{p_s}, \qquad \frac{d(\Delta p/p_s)}{dt} = \frac{e\hat{V}\omega_s}{2\pi\beta_s^2 E_s}[\sin\phi - \sin\phi_s] \tag{9.27}$$

If peak amplitudes are small the differential Eqs. 9.27 yield

$$\frac{d^2\Delta\phi}{dt^2} + \Omega_s^2 \Delta\phi = 0 \tag{9.28}$$

the motion is sinusoidal, with a synchrotron angular frequency

$$\Omega_s = \frac{c}{R}\sqrt{\frac{|\eta| hq\hat{V}\cos\phi_s}{2\pi E_s}} \tag{9.29}$$

The synchrotron tune, number of synchrotron oscillations per revolution, writes

$$\nu_s = \frac{\Omega_s}{\omega_{\text{rev}}} = \frac{1}{\beta_s}\sqrt{\frac{\eta hq\hat{V}\cos\phi_s}{2\pi E_s}} \tag{9.30}$$

Synchrotron oscillations are slow compared to betatron oscillations, typically $\nu_s \sim \nu_{\text{x,y}}/10^{2\sim 3}$. Motion stability requires $\Omega_s^2 > 0$, or

$$\eta\cos\phi_s > 0$$

Longitudinal motion in $(\phi, \dot\phi/\Omega_s)$ phase space is on a circle. The extent in phase and energy, or momentum, of the small amplitude oscillations satisfy

$$\widehat{\Delta\phi} = \frac{h\eta E_s}{p_s R\Omega_s}\frac{\widehat{\Delta E}}{E_s} = \frac{h\eta E_s}{p_s R\Omega_s}\beta_s^2\frac{\widehat{\Delta p}}{p_s} \tag{9.31}$$

The bunch length is

$$L_{\text{bunch}} = \frac{R}{h}\widehat{\Delta\phi} \tag{9.32}$$

Separatrix

If peak amplitudes are large the oscillations are non-linear and, assuming slow acceleration, by combining Eqs. 9.27,

$$\frac{d^2\Delta\phi}{dt^2} + \Omega_s^2\frac{\sin\phi - \sin\phi_s}{\cos\phi_s} = 0 \tag{9.33}$$

A first integral of this equation is the equation of the separatrix (Fig. 9.16)

$$\frac{\dot\phi^2}{2} - \Omega_s^2\frac{\cos\phi + \phi\sin\phi_s}{\cos\phi_s} = -\Omega_s^2\frac{\cos(\pi-\phi_s) + (\pi-\phi_s)\sin\phi_s}{\cos\phi_s} \tag{9.34}$$

This defines two locations where $\dot\phi$ changes sign, *i.e.* $\dot\phi = 0$, namely,
(i) $\phi_1 = \pi - \phi_s$,
(ii) ϕ_2 such that $\cos\phi_2 + \phi_2\sin\phi_s = \cos(\pi-\phi_s) + (\pi-\phi_s)\sin\phi_s$.

The motion is stable, oscillatory, within the domain $\phi \in [\phi_1, \phi_2]$, the "bucket", and unbounded beyond. The bucket height is obtained for $\phi = \phi_s$, namely, from Eq. 9.34

$$\frac{\dot\phi_{\max}}{\Omega_s} = \sqrt{2\left[2 - (\pi - 2\phi_s)\tan\phi_s\right]} \tag{9.35}$$

Expressed in momentum,

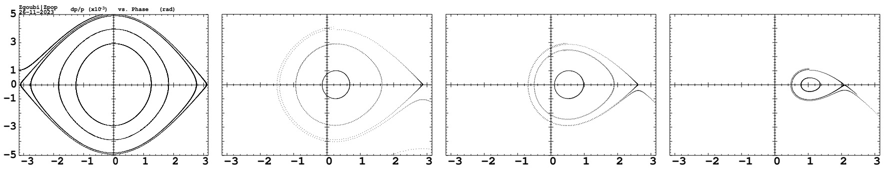

Fig. 9.16 Longitudinal motion separatrix in $(\phi, dp/p)$ phase space, and some stable as well as unbounded motions. Case of SATURNE 2 at injection energy, 50 MeV. From left to right: case of $\phi_s = 0$ (stationary bucket), $\phi_s = 15,\ 30$, and 60 deg. Small motions are centered on ϕ_s, their synchrotron tunes satisfy Eq. 9.30. The momentum acceptance (height of the separatrix) satisfies Eq. 9.36, with respectively $\pm\frac{\widehat{\Delta p}}{p_s} \approx 0.00496,\ 0.00392,\ 0.00290$ and 0.00107

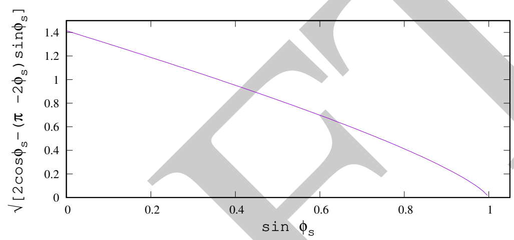

Fig. 9.17 Dependence of the momentum extent of the bucket $\left(\text{normalized to } \frac{1}{\beta_s}\sqrt{\frac{q\hat V}{\pi h \eta E_s}}\right)$ on the synchronous phase ϕ_s. It takes its value in $\sqrt{2} \to 0$ for $\sin\phi_s : 0 \to 1$

$$\pm\frac{\widehat{\Delta p}}{p_s} = \pm\frac{1}{\beta_s}\sqrt{\frac{q\hat V}{\pi h \eta E_s}\left[2\cos\phi_s - (\pi - 2\phi_s)\sin\phi_s\right]} \tag{9.36}$$

Its dependence on ϕ_s is represented in Fig. 9.17. Stationary bucket mode, *i.e.* $\sin\phi_s = 0$, has greatest acceptance. The latter decreases in accelerated bucket mode as $\phi_s \to \pi/2$ (Fig. 9.16).

Adiabatic damping of synchrotron oscillations

The equation of motion, Eq. 9.33, assumes a slow acceleration rate, $dT_{\text{rev}}/dt \ll 1$, such that $p_s(t)$, η, possibly $\hat V$, and thus Ω_s change slowly during synchrotron oscillations and therefore can be considered constant. The extreme phase and momentum excursions during acceleration satisfy

$$\begin{aligned} \widehat{\Delta\phi} &\propto \left(\frac{\eta}{R^2\gamma\hat V\cos\phi_s}\right)^{1/4} \\ \frac{\widehat{\Delta p}}{p_s} &\propto \frac{1}{\beta_s}\left(\frac{\hat V\cos\phi_s}{\eta\gamma^3 R^2}\right)^{1/4} \end{aligned} \tag{9.37}$$

In the case of acceleration on a fixed orbit (constant radius R),

$$\widehat{\Delta\phi} \times \widehat{\Delta p} = \text{constant} \tag{9.38}$$

Adiabatic damping of the betatron oscillations

The mechanism is described in Sect. 8.2.2 (Fig. 8.14), the equations of motion are addressed in Sect. 10.2.3. In the case of an adiabatic change of momentum $p = \beta\gamma m_0 c$ (a slow change compared to the betatron motion oscillation frequency) the transverse motion damping satisfies

$$p\,\varepsilon_u = \text{constant}, \quad \text{or} \quad \beta\gamma\varepsilon_u = \text{constant} \tag{9.39}$$

Coordinate damping satisfies (Eq. 10.22 with orbit radius R =constant)

$$x, y \propto 1/\sqrt{p}, \qquad x', y' \propto 1/\sqrt{p} \tag{9.40}$$

9.2.5 Synchrotron Radiation, Dynamical Effects

Emittance growth upon SR matters in high γ rings, electron rings so far, muon collider possibly in the future [30] and other FCC lepton and hadron collider [8].

The stochastic nature of SR and the energy loss it results in, have been introduced in Chap. 5. Dynamical effects in a synchrotron ring are further addressed here [31, 32].

Motion invariants

In the absence of perturbation by synchrotron radiation, particle motion satisfies the Courant-Snyder (Eq. 9.41) and longitudinal (Eq. 9.42) phase-space invariants

$$\varepsilon_u = \gamma_u(s)u^2 + 2\alpha_u(s)uu' + \beta_u(s)u'^2 \;\; (u \; = \; x \; or \; y) \tag{9.41}$$

$$\varepsilon_l = \frac{\alpha E_s}{2\,\Omega_s}\left(\frac{\widehat{\delta E}}{E_s}\right)^2 \tag{9.42}$$

Under the effect of stochastic SR, individual invariants can in general not be determined, averages over particle ensembles are considered instead (noted $\overline{(*)}$ in the following), they evolve according to

$$\frac{d\overline{\varepsilon}_u}{dt} = -\frac{\overline{\varepsilon}_u}{\tau_u} + C_u \tag{9.43}$$

towards a stationary solution

$$\varepsilon_{n,eq} = C_u\,\tau_u \tag{9.44}$$

where C_u is a constant at fixed energy (storage ring), with characteristic time

$$\tau_u = \frac{T_{rev}\, E_s}{U_s\, J_u} \tag{9.45}$$

$J_{n=x,y,l}$ are the partition numbers (lattice properties), respectively horizontal, vertical, longitudinal,

$$J_x = 1 - \mathcal{D}, \quad J_y = 1, \quad J_l = 2 + \mathcal{D} \tag{9.46}$$

where

$$\mathcal{D} = \frac{\overline{D_x(1-2n)/\rho^3}}{\overline{1/\rho^2}}$$

In this expression, $\overline{(*)} = \frac{1}{2\pi R}\int_{\text{dipoles}}(*)ds$, n is the field index - case of combined function dipoles, D_x is the dispersion function, The partition numbers satisfy the Robinson theorem

$$J_x + J_y + J_l = 4 \tag{9.47}$$

Table 9.1 Common expressions for the energy loss per turn, U_s (E-loss), for the damping times and equilibrium emittances, in the hypothesis of an isomagnetic lattice. Their scaling with γ is given in the 2nd row

	E-loss	$\varepsilon_{l,eq}$	σ_l	τ_l	$\varepsilon_{x,eq}$ [1]	τ_x	$\varepsilon_{y,eq}$	τ_y
Scaling :	$\boldsymbol{\gamma^4}$	$\boldsymbol{\gamma^{3/2}}$	$\boldsymbol{1/\gamma^{1/2}}$	$\boldsymbol{1/\gamma^3}$	$\boldsymbol{\gamma^2}$	$\boldsymbol{1/\gamma^3}$		$\boldsymbol{1/\gamma^3}$
	$C_\gamma \frac{E_s^4}{\rho}$	$\frac{\alpha E_s}{\Omega_s}\frac{C_q\gamma^2}{J_l\,\rho}$	$\frac{\alpha c}{\Omega_s}\sigma_{\frac{\Delta E}{E}}$	$\frac{T_{rev}E_s}{U_s J_l}$	$\frac{C_q\gamma^2}{J_x\rho}\overline{\mathcal{H}}$	$\frac{T_{rev}E_s}{U_s J_x}$	$\ll \varepsilon_x$	$\frac{T_{rev}E_s}{U_s J_y}$

[1] $\overline{\mathcal{H}} = \frac{1}{L_{\text{dip}}}\int_{\text{dip}}\frac{ds}{\beta_x}\left[D_x^2 + (\alpha_x D_x + \beta_x D_x')^2\right]$, integral over the dipoles.

Common expressions for the calculation of the energy loss and equilibrium quantities, in the hypothesis of an isomagnetic lattice, are recalled in Tab. 9.1.

Vertical emittance results from coupling, always present in a ring, due for instance to a loss of median plane symmetry, or to fringe fields, or excited on purpose to control the vertical emittance as in light sources. Given the coupling factor κ - normally < 0.1, the vertical and horizontal emittances satisfy

$$\epsilon_y = \kappa\epsilon_x, \qquad \epsilon_x + \epsilon_y = \epsilon_0 \tag{9.48}$$

where ϵ_0 is the equilibrium horizontal emittance in the absence of coupling (Tab. 9.1).

The basic considerations above hold for a defect-free planar ring. Things can be (as usual) more complicated, for instance in the presence of vertical dispersion.

Field scaling

Particle stiffness decrease upon SR loss causes these to experience increased field strength ($1/\rho$ in dipoles, $G/B\rho$ in quadrupoles, etc.). In the case of beam lines (which may include high energy ERLs [11]), this effect may be taken care of by scaling the magnetic fields to the theoretical average energy loss (Eq. 5.12), namely

$$\Delta E_{scaling} = \sum_{bends} \frac{2}{3} r_0 e c \gamma^3 B \Delta\theta \tag{9.49}$$

In a storage ring the energy lost by SR is restored by the RF system, bends and lenses are operated at constant field. In pulsed regime such as in a booster injector, bends and lenses are operated at constant strength during acceleration.

9.2.6 Visible Synchrotron Radiation. Interference

Visible SR was first observed at the GEC 70 MeV. For this reason it has been introduced in the Weak Focusing Synchrotron chapter, Sect. 8.2.3. The SR spectrum at that energy peaks - has its critical frequency - in the visible region. The matter is developed further in the present chapter, in regard with the use of visible SR for beam diagnostics in electron and high energy proton rings [31, 33].

An example of the use of visible SR from a proton beam is found at the CERN SPS, where edge radiation was used at 270 GeV for beam imaging [34]. At that energy in the SPS, the critical frequency (the peak brightness) is in the infrared region. Undulator radiation, more intense, was used down to 200 GeV [35], in the $\mathrm{p}-\overline{\mathrm{p}}$ collider era (1980s). Another example is the LHC synchrotron light profile monitor, a major beam monitoring tool at injection energy, 450 GeV [36][37, Appendix C].

An example of the use of visible SR from a high energy electron beam is found at the former LEP, where it was produced in a dedicated 4-dipole miniwiggler. The critical frequency in a high energy electron ring is way above the visible range. In such case, visible SR can be dealt with in terms of low-frequency SR [38], a method which can be extended to the analytical treatment of SR interference [37]. The underlying theoretical material is recalled here. It is resorted to in the exercises, to cross check Poynting computation from raytracing (using Eq. 8.36).

Low frequency SR

A typical electric field impulse from a LEP miniwiggler dipole, and the resulting spectral brightness, as observed in the laboratory, are displayed in Fig. 9.18. The LEP 4-dipole miniwiggler was subject to visible light interference from 4 coherent sources, the effect is illustrated in Fig. 9.19.

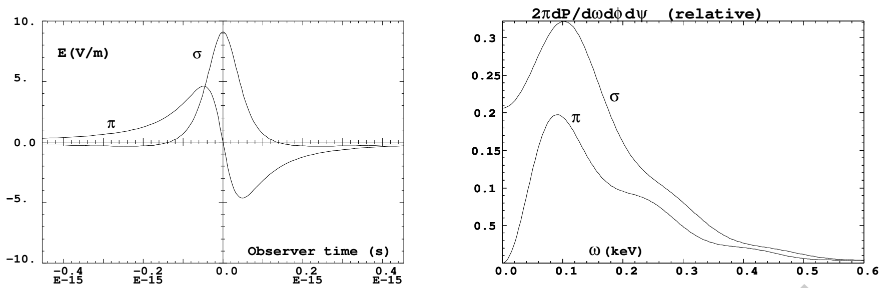

Fig. 9.18 Left: typical shape of the $E_\sigma(\tau)$ and $E_\pi(t)$ electric impulse components of the Poynting vector, emitted by a 2.5 GeV electron on a $\rho = 53.6$ m circular trajectory in a $l = 20$ cm-long dipole, as observed in the laboratory. $E_{\sigma,\,\pi}(\tau)$ are obtained from the stepwise integration of electron motion through the magnet, which provides the ingredients to compute Eq. 8.36, accounting for the retarded time $t = \tau - r(t)/c$ (Eq. 8.37). Right: the spectral brightness of the σ component of the radiation allows comfortable beam diagnostics conditions in the visible range ($\omega \sim 0.5$ eV)

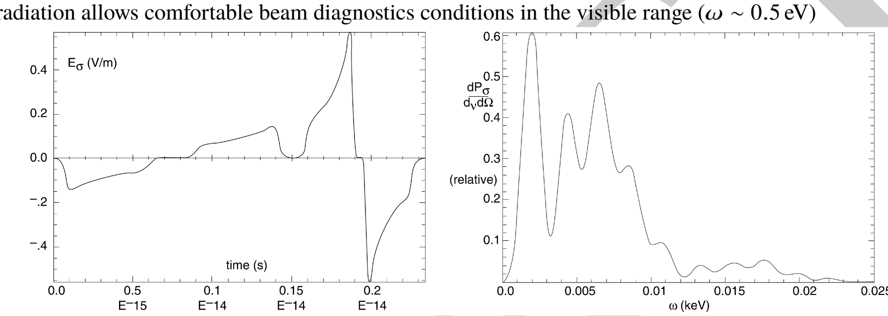

Fig. 9.19 An interferencial spectrum, case of LEP 4-dipole miniwiggler [39]. By contrast with the single dipole case (Fig. 9.18), the spectral brightness of the σ component cancels in the low energy end of the spectrum

A doublet of LEP miniwiggler dipoles, in both cases of same sign and opposite sign dipoles, is the object of numerical simulations in exercise 9.6. It is on the other hand treated theoretically in [37, Sect. 3.1]. The latter provides all necessary material for cross checks of numerical outcomes from the stepwise integration of electron motion,

9.2.7 Polarization, Resonances

In a weak focusing optics lattice, radial field components experienced by a particle in the course of its vertical betatron motion are small, which results in weak depolarizing resonances (Sect. 8.2.4). By contrast, strong focusing field gradients in the combined function dipoles and/or focusing lenses of strong focusing optics results in strong radial field components and therefore strong depolarizing resonances.

Spin precession and resonant spin motion in the magnetic components of a cyclic accelerator have been introduced in Sects. 3.2.5, 4.2.5. The general conditions for depolarizing resonance to occur have been introduced in Sect. 8.2.4. In a strong focusing synchrotron they essentially result from the radial field components in the focusing magnets and their strength is determined by the lattice optics, as follows.

Strength of imperfection resonances

Imperfection, or integer, depolarizing resonances are driven by a non-vanishing vertical closed orbit $y_{\rm co}(\theta)$ which causes spins to experience periodic radial fields in focusing magnets, dipoles in combined function lattices and quadrupoles in separated function lattices, namely,

$$B_x(\theta) = G\, y(\theta) = K(\theta) \times B_0\rho_0 \times y_{\rm co}(\theta) \tag{9.50}$$

with θ the orbital angle and $B_0\rho_0$ the lattice rigidity. Resonance occurs if the spin undergoes an integer number of precessions over a turn: it then experiences 1-turn-periodic torques, which cause it to move away from the stable $\mathbf{n}_0$ direction as field perturbations along the closed orbit add up coherently. Thus resonances occur at integer values

$$G\gamma_n = n$$

A Fourier development of these perturbative fields yields the strength of the $G\gamma_n$ harmonic [40, Sect. 2.3.5.1]

$$\epsilon_n^{\rm imp} = (1 + G\gamma)\frac{R}{2\pi} \oint K(\theta)\ y_{\rm co}(\theta)\, e^{-jG\gamma(\theta-\alpha)}\ e^{jn\theta}\, d\theta$$

In the thin-lens approximation, near the resonance where $G\gamma - n \to 0$, this simplifies into a series over the quadrupole fields,

$$\epsilon_n^{\rm imp} = \frac{1 + G\gamma_n}{2\pi} \sum_{\rm Qpoles} \left[\cos G\gamma_n\, \alpha_i + \sin G\gamma_n\, \alpha_i\right] (KL)_i\ y_{\rm co}(\theta_i) \tag{9.51}$$

with θ_i the quadrupole location, $(KL)_i$ the integrated strength (slice the dipoles as necessary in an AG lattice for this series to converge) and α_i the cumulated orbit deviation.

Orbit harmonics near the betatron tune ($n = G\gamma_n \approx \nu_y$) excite strong resonances. Imperfection resonance strength is further amplified in P-superperiodic rings, with m-cell superperiods, if the betatron tune $\nu_y \approx$ integer $\times\, m \times P$ [41, Chap.3-I].

Strength of intrinsic resonances

Intrinsic depolarizing resonances are driven by betatron motion, which causes spins to experience strong radial field components in quadrupoles, namely

$$B_x(\theta) = G\, y(\theta) = K(\theta) \times B_0\rho_0 \times y_\beta(\theta) \tag{9.52}$$

The effect of resonances on spin depends upon betatron amplitude and phase, their effect on beam polarization depends on beam emittance. Longitudinal fields from dipole ends are usually weak by comparison and ignored. The location of intrinsic resonances depends on betatron tune, it is given in an M-periodic structure by

$$G\gamma_n = nM \pm \nu_y$$

A Fourier development of the perturbative fields yields the two families of strengths [40, Sect. 2.3.5.2]

$$\epsilon_n^{\mathrm{intr}\pm} = \frac{\lambda_x\rho_0}{4\pi}\int_0^{2\pi} K(\theta)\sqrt{\beta_y(\theta)\frac{\varepsilon_y}{\pi}}\, e^{\pm j\left(\int_0^{s(\theta)}\frac{ds}{\beta_y} - \nu_y\theta\right)}\, e^{-jG\gamma(\theta-\alpha(\theta))}\, e^{jn\theta}\, d\theta$$

In the thin-lens approximation, near the resonance where $G\gamma \pm \nu_y - n \to 0$, this simplifies into a series over the quadrupole fields,

$$\left\{\begin{array}{c}\mathcal{R}e(\epsilon_n^{\mathrm{intr}\pm}) + \\ j\,\mathcal{I}m(\epsilon_n^{\mathrm{intr}\pm})\end{array}\right\} = \frac{1+G\gamma_n}{4\pi}\sum_{\mathrm{Qpoles}}\left\{\begin{array}{l}\cos(G\gamma_n\alpha_i \pm \varphi_i) + \\ j\,\sin(G\gamma_n\alpha_i \pm \varphi_i)\end{array}\right\}(KL)_i\sqrt{\beta_{y,i}\frac{\varepsilon_y}{\pi}} \tag{9.53}$$

Spin diffusion

Spin diffusion stems from the stochastic emission of photons in magnetic fields (Sect. 5.2.3.1). A change δ in the energy offset ΔE of a particle, due to the emission of a photon, causes a change $\partial\mathbf{n}/\partial\delta$ of the local spin precession direction. In dispersive sections it also causes a change in the horizontal invariant, $\partial\epsilon_x/\partial\delta$, and in vertical invariant as well, $\partial\epsilon_y/\partial\delta$ in the presence of vertical dispersion, which in turn result in perturbations $\partial\mathbf{n}/\partial\epsilon_{x,y}$.

As far as numerical integration is concerned, spin diffusion is a sub-product of the stepwise integration of Thomas-BMT equation (Sect. 3.2.5), and of the simulation of stochastic emission of photons (Sect. 5.2.3.1). It is at work in Cornell RCS simulation, exercise 9.4.

9.3 Exercises

In complement to the present exercises, a tutorial on depolarizing resonances in a strong focusing synchrotron can be found in [40, Chap. 14]. Proton, helion and electron beams are considered, using the lattice of the AGS Booster at BNL. The simulations explore methods for preservation of polarization, including tune-jump quadrupoles, a solenoid, Siberian snakes, spin rotators in the case of electrons, including synchrotron radiation and effects on polarization life time.

Note: input data files for these simulations are available in `zgoubi` sourceforge repository at
https://sourceforge.net/p/zgoubi/code/HEAD/tree/branches/exemples/book/zgoubiMaterial/synchrotron_strongFocusing/

9.1 Construct SATURNE 2 Synchrotron

Solution: page **??**

Over the years 1978-1997 the 3 GeV synchrotron SATURNE 2 at Saclay (Figs. 9.3, 9.20) delivered polarized proton beams, and polarized deuteron and ^{6}Li beams up to 1.1 GeV/nucleon, for intermediate energy nuclear physics research, including meson production [45, 42, 43]. The separated function synchrotron was designed *ab initio* for the acceleration of polarized ion beams [44], and the first strong focusing synchrotron to do so - ZGS, first to accelerate polarized beams, protons and deuterons, was a weak focusing synchrotron (Chap. 8).

SATURNE 2 is a FODO lattice with missing dipole. Its parameters are given in Tab. 9.2.

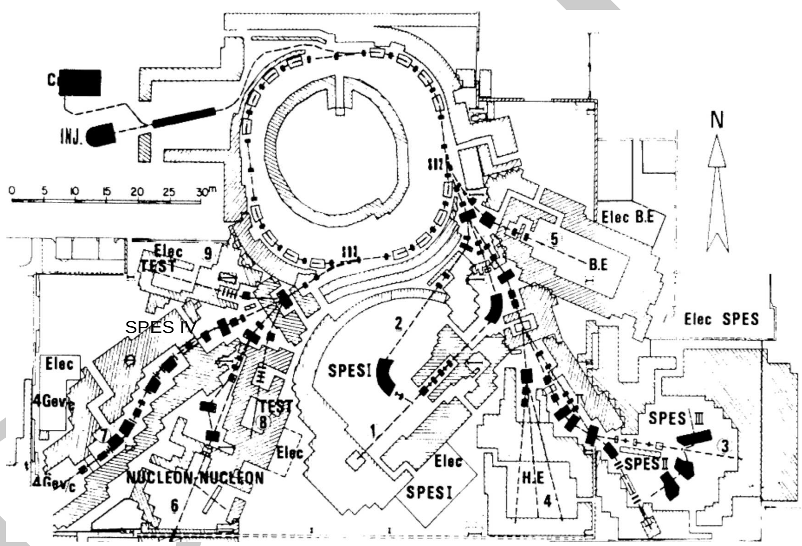

Fig. 9.20 SATURNE 2 synchrotron and its experimental areas, including mass spectrometers SPES I to SPES IV, a typical nuclear physics accelerator facility. The polarized ion sources Dioné and Hypérion are at the top left, followed by a 20 MeV linac. In the early 1980s a synchrotron booster, MIMAS, was added for higher polarized ion performance

(a) Simulate the main dipole using BEND. Dipole fringe fields matter in this small ring, take them into account assuming $\lambda = 8$ cm extent and the following Enge coefficient values (Eq. 14.11, Sect. 14.3.3):

Table 9.2 Parameters of SATURNE 2 separated function FODO lattice. ρ_0 is the radius of the reference orbit in the main dipole

Orbit length, C	m	105.5556
Average radius, $R = C/2\pi$	m	16.8
Straight sections, length:		
- short	m	0.716256
- long	m	3.92148
Dipole:		
- bend angle, α	deg	22.5
- magnetic radius, ρ_0	m	6.3381
- wedge angle, ε	deg	2.45
Quadrupole:		
- gradient range	T/m	0.5 - 10.56
- magnetic length F/D	m	0.46723 / 0.486273
Wave numbers, typical, ν_x; ν_y		3.64; 3.60
Chromaticities, ξ_x; ξ_y		negative, a few units
Momentum compaction α		0.015
Injection energy (proton)	MeV	20
Top energy	GeV	3
$\dot{B}$	T/s	4.2
Synchronous energy gain	keV/turn	1.160
RF harmonic		2

$$C_0 = 0.2401,\ C_1 = 1.8639,\ C_2 = -0.5572,\ C_3 = 0.3904,\ C_4 = C_5 = 0$$

Produce the transport matrix of the dipole, check against theory. Compare with the matrix of the hard edge model.

Produce a graph of the field across the dipole, in the median plane and at 5 cm vertical distance. OPTIONS[CONSTY=ON] can be used to force a particle to constant Y and Z.

Simulate the F and D quadrupoles, using respectively QUADRUPOLE and MULTIPOL. Compare matrices with theory.

Construct the cell. Produce machine parameters (tunes, chromaticities), check against data, Tab. 9.2.

Construct the 4-cell ring. Produce a graph of the optical functions. Produce the beam matrix.

(b) Accelerate a bunch comprised of a few tens of particles with Gaussian density distributions (it can be defined using MCOBJET), from injection to top energy, 50 MeV to 3 GeV. Use harmonic 3 RF frequency, take a (unrealistic, for a reduced number of turns) peak RF voltage $\hat{V} = 1$ MV, and synchronous phase $\phi_s = 30$ deg.

Produce a graph of Y, Z and dp/p versus turn. Check the transverse damping against theory.

(c) Determine the momentum acceptance of the ring at 50 MeV, with $\hat{V} = 10$ kV peak voltage, in the following four cases: stationary bucket (synchronous phase $\phi_s = 0$) and accelerated buckets with $\phi_s = 15,\ 30,$ and 60 deg.

Reproduce the longitudinal phase space graphs displayed in Fig. 9.16.

9.2 Non-Linear Motion in SATURNE 2

Solution: page **??**

(a) Simulate horizontal particle motion near a third integer resonance. Provide a graph of the transverse phase space.

(b) Simulate horizontal particle motion near a quarter integer resonance. Provide a graph of the transverse phase space.

9.3 SVD Orbit Correction

Solution: page **??**

Using SATURNE 2 ring, inject dipole defects and use SVDOC to find the corrected orbit.

It can be done in the following way:

- place a horizontal pickup (HPU), a dipole defect (HDEF, using a thin-lens MULTIPOL, length *e.g.* 1e-3 cm) and a dipole corrector (HKIC, using a thin-lens MULTIPOL) in the middle of the QF quadrupole of the FODO cells,
- in a similar manner, place a VPU, a VDEF and a VKIC just upstream of the FODO cell QD,
- excite V and H closed orbits by injecting random defects in HKIC and VKIC, using ERRORS.

Use SVDOC to find the orbit correction.

Provide a graph of the orbit at the PUs, before and after correction.

In the previous setting, there is 24 defects (12 H and 12 V) and 24 correctors (12 H and 12 V). Repeat for 24 defects and only 12 correctors per plane.

9.4 Cornell Electron RCS. Radiative Energy Loss

Solution: page **??**

Note: details regarding these simulations and their solutions can be found in the Tech. Note EIC/57;BNL-114452-2017-IR [46].

The goal in this exercise is to simulate Cornell RCS lattice and accelerate beam, first without synchrotron radiation, then taking it into account. In a fourth step electron spin is added and polarization transmission through the acceleration cycle assessed.

(a) Details of the RCS geometry and lattice can be found in Ref. [14], however a simplified 6-superperiodic version of the ring is considered here, with six identical long straights and six identical arcs. The RCS parameters are given in Tab. 9.3. The input data files are given in

- Tabs. 9.4 and 9.5: definition of the focusing and defocusing bends, and of the focusing and defocusing doublets;
- Tab. 9.6: definition of a FODO cell;
- Tab. 9.7: definition of a supercell;
- Tab. 9.8: definition of the 6-supercell ring.

Produce the optical parameters of the ring. A TWISS command can be used for that. Produce graphs of the closed orbit and optical functions around the ring.

(b) Raytrace a few tens of particles over 2300 turns around the ring, from 320 MeV to 8 GeV about, ignoring radiative energy loss. Assume normalized emittances $\varepsilon_x =$

Table 9.3 Cornell RCS parameters in the present simplified lattice simulation

Top energy	GeV	7
Injection energy	MeV	320
Circumference, simplified 6-supercell case	m	786.947
Bunch		
ε_x, ε_y at injection	$\pi\mu$m	25
Bunch length	mm	6
dE/E at injection		$5\,10^{-3}$
Combined function lattice		48×FFDD
Nb of F and D cell dipoles		192
ρ_F, ρ_D	m	≈95, 92
Field at 7 GeV	T	0.25
Max. β_x, β_y	m	29, 26
ν_x, ν_y, natural		9.62, 13.82
ξ_x, ξ_y, natural		-13, -16
RF, synch. radiation		
Repetition rate	Hz	up to 60
Acceleration rate	MV/turn	3
E-loss per turn at 5, 10 GeV	MeV	0.6, 9
τ_x ($\approx \frac{2.5}{E^3}$) at 5, 10 GeV	ms	16, 2

$\varepsilon_y = 25\pi\mu$m, Gaussian densities, initial *rms* $\delta p/p = 5\,10^{-3}$. Use CAVITE[IOPT=3] for acceleration. Produce a graph of the three phase spaces. produce graphs of transverse and longitudinal excursions versus turn number, check damping again expectations.

(c) Re-do (b) with synchrotron radiation energy loss, following SR loss theoretical material introduced in the "Betatron" Chap. 5. Use SRLOSS for radiation, and CAVITE[IOPT=11,Facility=CornellSynch,$U_{00} = 9.48145321 \times 10^{-6}$] for acceleration. Check equilibrium emittances.

(d) Produce a graph of the average bunch polarization over the acceleration cycle in (c), starting with all spins up at injection energy. Check against the resonance spectrum over $a\gamma$: $0.7 \rightarrow 18$.

Table 9.4 Simulation input data files for the focusing (left) and defocusing (right) combined function dipoles. They define the segments, respectively, F_BEND_S:F_BEND_E and D_BEND_S:D_BEND_E, for use by INCLUDE commands in further input data files. These files can be run as is: FIT will center the closed orbit across the magnet, accounting for the field scaling by the *ad hoc* coefficient under SCALING

```
RCS focusing combined function dipole
! File: F_BEND.inc
'OBJET'
1. *1e3
5
.001 .001 .001 .001 0. .0001
0. 0. 0. 0. 0. 1.

'SCALING'
1  1
MULTIPOL F_BEND
-1
0.98523998
1

'MARKER'  F_BEND_S

'MULTIPOL'   F_BEND
0  .Dip
320.2700  10. 0.1021746 0.0435214 0. 0. 0. 0. 0. 0. 0. 0.
0. 0. 10.00  4.0  0.800 0.00 0.00 0.00 0.00 0. 0. 0. 0.
4  .1455   2.2670  -.6395  1.1558  0. 0.  0.
0. 0. 10.00  4.0  0.800 0.00 0.00 0.00 0.00 0. 0. 0. 0.
4  .1455   2.2670  -.6395  1.1558  0. 0.  0.
0. 0. 0. 0. 0. 0. 0. 0. 0. 0.
#30|320|30         ! YCE offset found by FIT
3   0.0000000000E+00 0.52818473  -1.6362461735E-02

'MARKER'  F_BEND_E

'FIT'
1
4 65 0 [-4.,4.]
2
3.1 1 2 #End 0. 1. 0
3.1 1 3 #End 0. 1. 0

'END'
```

```
RCS defocusing combined function dipole
! File: D_BEND.inc
'OBJET'
1. *1e3
5
.001 .001 .001 .001 0. .0001
0. 0. 0. 0. 0. 1.

'SCALING'
1  1
MULTIPOL D_BEND
-1
1.1078694
1

'MARKER'  D_BEND_S

'MULTIPOL'   D_BEND
0  .Dip
320.0150 10. 0.1022560 -0.0437325 0. 0. 0. 0. 0. 0. 0. 0.
0. 0. 10.00  4.0  0.800 0.00 0.00 0.00 0.00 0. 0. 0. 0.
4  .1455   2.2670  -.6395  1.1558  0. 0.  0.
0. 0. 10.00  4.0  0.800 0.00 0.00 0.00 0.00 0. 0. 0. 0.
4  .1455   2.2670  -.6395  1.1558  0. 0.  0.
0. 0. 0. 0. 0. 0. 0. 0. 0. 0.
#30|320|30         ! YCE offset found by FIT
3   0.0000000000E+00  -1.4110319  -1.6362461735E-02

'MARKER'  D_BEND_E

'FIT'
1
4 65 0 [-2.,2.]
2
3.1 1 2 #End 0. 1. 0
3.1 1 3 #End 0. 1. 0

'END'
```

Table 9.5 definition of focusing (left) and defocusing (right) doublets, for use by further INCLUDE commands

```
! File: BF2.inc

'MARKER' BF2_S

'DRIFT'
23.999061
'INCLUDE'
1
F_BEND.inc[F_BEND_S:F_BEND_E]
 'DRIFT'
23.999061
 'DRIFT'
23.999061
'INCLUDE'
1
F_BEND.inc[F_BEND_S:F_BEND_E]
 'DRIFT'
23.999061

'MARKER' BF2_E

'END'
```

```
! File: BD2.inc

'MARKER' BD2_S

'DRIFT'
24.126561
'INCLUDE'
1
D_BEND.inc[D_BEND_S:D_BEND_E]
 'DRIFT'
24.126561
 'DRIFT'
24.126561
'INCLUDE'
1
D_BEND.inc[D_BEND_S:D_BEND_E]
 'DRIFT'
24.126561

'MARKER' BD2_E

'END'
```

Table 9.6 Simulation input data file for a FODO cell

```
! File: FD.inc

'MARKER'  FD_S
'INCLUDE'
1
BF2.inc[BF2_S:BF2_E]
'INCLUDE'
1
BD2.inc[BD2_S:BD2_E]
'MARKER'  FD_E
'END'
```

Table 9.7 Simulation input data file for a supercell

```
File : superCell.inc
'OBJET'
1. *1e3                 ! Rigidity is 1 T m.
5
.001 .001 .001 .001 0. .0001
0. 0. 0. 0. 0. 1.

'MARKER'  superCell_S

'INCLUDE'
1
F_BEND.inc[F_BEND_S:F_BEND_E]
 'DRIFT'
40.988209
 'DRIFT'
40.988209
'INCLUDE'
1
F_BEND.inc[F_BEND_S:F_BEND_E]
 'DRIFT'
15.600113
'DRIFT'
15.600113
'INCLUDE'
1
D_BEND.inc[D_BEND_S:D_BEND_E]
 'DRIFT'
24.062811
'DRIFT'
24.062811
'INCLUDE'
1
D_BEND.inc[D_BEND_S:D_BEND_E]
 'DRIFT'
15.600113
'DRIFT'
15.600113
'INCLUDE'
1
F_BEND.inc[F_BEND_S:F_BEND_E]
 'DRIFT'
40.988209
'DRIFT'
40.988209
'INCLUDE'
1
F_BEND.inc[F_BEND_S:F_BEND_E]
 'DRIFT'
15.600113
'INCLUDE'
1
D_BEND.inc[D_BEND_S:D_BEND_E]
'DRIFT'
15.600113
'DRIFT'
15.600113
'INCLUDE'
1
D_BEND.inc[D_BEND_S:D_BEND_E]
 'DRIFT'
40.988209
'DRIFT'
40.988209
'INCLUDE'
1
F_BEND.inc[F_BEND_S:F_BEND_E]
 'DRIFT'
15.600113
 'DRIFT'
15.600113
'INCLUDE'
1
F_BEND.inc[F_BEND_S:F_BEND_E]
 'DRIFT'
24.062811
'INCLUDE'
1
BD2.inc[BD2_S:BD2_E]
'DRIFT'
24.062811
 'MULTIPOL'
0  .Dip
44.6375  10. 0.1022198 -0.0437325 0. 0.0 0.0 0.0 0.0 0.0 0.0 0.0
0. 0. 10.00  4.0  0.800 0.00 0.00 0.00 0.00 0. 0. 0. 0.
4  .1455   2.2670  -.6395  1.1558  0. 0.  0.
0. 0. 10.00  4.0  0.800 0.00 0.00 0.00 0.00 0. 0. 0. 0.
4  .1455   2.2670  -.6395  1.1558  0. 0.  0.
0. 0. 0. 0. 0. 0. 0. 0. 0. 0.
#30|45|30    Dip  B129VA
3   0.0000000000E+00  1.77777778E-02  -2.2814180400E-03
 'MULTIPOL'
0  .Dip
275.505  10. 0.1022165  0.0842350 0. 0.0 0.0 0.0 0.0 0.0 0.0 0.0
0. 0. 10.00  4.0  0.800 0.00 0.00 0.00 0.00 0. 0. 0. 0.
4  .1455   2.2670  -.6395  1.1558  0. 0.  0.
0. 0. 10.00  4.0  0.800 0.00 0.00 0.00 0.00 0. 0. 0. 0.
4  .1455   2.2670  -.6395  1.1558  0. 0.  0.
0. 0. 0. 0. 0. 0. 0. 0. 0. 0.
#30|276|30    Dip  B129HB
3   0.0000000000E+00   0.65358025  -1.4081043695E-02
 'DRIFT'
24.062811

 'DRIFT'
60.800000
 'DRIFT'
244.000000
 'DRIFT'
244.000000
 'DRIFT'
60.800000

'DRIFT'
24.062811
'MULTIPOL'
0  .Dip
275.505  10. 0.1022165 -0.0844460  0. 0.0 0.0 0.0 0.0 0.0 0.0 0.0
0. 0. 10.00  4.0  0.800 0.00 0.00 0.00 0.00 0. 0. 0. 0.
4  .1455   2.2670  -.6395  1.1558  0. 0.  0.
0. 0. 10.00  4.0  0.800 0.00 0.00 0.00 0.00 0. 0. 0. 0.
4  .1455   2.2670  -.6395  1.1558  0. 0.  0.
0. 0. 0. 0. 0. 0. 0. 0. 0. 0.
#30|276|30    Dip  B128VA
3   0.0000000000E+00   0.6397805  -1.4081043695E-02
 'MULTIPOL'
0  .Dip
44.6375  10. 0.1022198  0.0435214  0. 0.0 0.0 0.0 0.0 0.0 0.0 0.0
0. 0. 10.00  4.0  0.800 0.00 0.00 0.00 0.00 0. 0. 0. 0.
4  .1455   2.2670  -.6395  1.1558  0. 0.  0.
0. 0. 10.00  4.0  0.800 0.00 0.00 0.00 0.00 0. 0. 0. 0.
4  .1455   2.2670  -.6395  1.1558  0. 0.  0.
0. 0. 0. 0. 0. 0. 0. 0. 0. 0.
#30|45|30   Dip  B128HB
3   0.0000000000E+00  1.77777778E-02  -2.2814180400E-03
 'DRIFT'
24.062811

'INCLUDE'
1
5 * FD.inc[FD_S:FD_E]
'DRIFT'
7.073665   ! -24.126561 + 2*15.600113

'MARKER'  superCell_E

 'TWISS'
2  1. 1.

'SYSTEM'
1
gnuplot <./gnuplot_TWISS.gnu

'END'
```

Table 9.8 Simulation input data file for Cornell RCS ring

```
File: ring.INC.dat. Cornell RCS ring
'OBJET'
1. *1e3
5
.001 .001 .001 .001 0. .0001
0. 0. 0. 0. 0. 1.

'OPTIONS'
1 1
WRITE OFF

'SCALING'
1  3
MULTIPOL
-1
1.
1
MULTIPOL F_BEND
-1
0.99292280
1
MULTIPOL D_BEND
-1
1.1294084
1
```

```
'INCLUDE'
1
6 * superCell.inc[superCell_S:superCell_E]

'OPTIONS'
1 1
WRITE ON

!'TWISS'        ! Uncomment to get a TWISS and graphs.
!2  1. 1.
!'SYSTEM'
!1
!gnuplot <./gnuplot_TWISS.gnu
!'END'

'FIT2' ! Set SCALING coefficients for requested tunes.
2
3  8 0 .2
3 12 0 .2
2
0.1 7 0 #End 0.62 1. 0
0.1 8 0 #End 0.82 1. 0

!'MATRIX'
!1 11
'TWISS'
2 1. 1.
'END'
```

9.5 Coupling in a Light Source Storage Ring

In this exercise, it is proposed to reproduce SR damping simulations, in a case of coupled light source lattice, detailed in JINST article [48]

Simulation of radiation damping in rings, using stepwise ray-tracing methods (the original (1990s) ESRF lattice is concerned - today's ESRF lattice is completely different, minimal emittance, un-isomagnetic).

An input data file for the early ESRF lattice can be found at

https://sourceforge.net/p/zgoubi/code/HEAD/tree/
branches/exemples/SRDamping/ESRFRing/coupled

It accounts for $\kappa = 0.58$ optical coupling, by a single skew quadrupole placed at the begining of the lattice.

Reproduce the numerical results for this coupled case, as detailed in Sect. 5 of that JINST article [48].

9.6 SR Electric Impulse and Interference in a Miniwiggler

Solution: page **??**

In this exercise, the electric field component of synchrotron radiation in short dipoles is produced. An interferential spectrum is prodcued from a pair of dipoles. This exercise is based on the LEP miniwigler configuration [37].

(a) Produce the input data file for the simulation of an electron trajectory in one of the LEP miniwiggler dipoles schemed in Fig. 9.21. Dipole length is $L = 52.602$ cm, bend angle 0.8 mrad. Electron energy is $E = 45$ GeV. Produce the electric field impulse observed at long distance in the direction $\phi = \psi = 0$. Produce its spectrum.

Check the various quantities: duration of the electric field impulse, critical frequency of the spectrum, etc.

(b) Consider the dipole pair of 9.21. Take distance between dipoles $d = 23.098$. Produce the electric field impulse observed at long distance in the direction $\phi = \psi = 0$. Produce its spectrum.

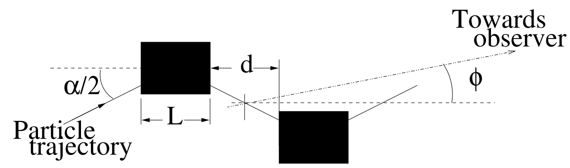

Fig. 9.21 Synchrotron radiation electric field impulse from a pair of dipoles is observed in the direction (ϕ, ψ), with ϕ the bend plane angle as shown, and ψ the angle to the bend plane. This schematic defines the observation direction $\phi = 0$

Check the various quantites: duration of the electric field impulse, critical frequency of the spectrum.

Repeat, in the direction $\phi = 0,\ \psi = 0.2$ mrad.

(c) Repeat (b), for the dipole pair disposed as in Fig. 9.21 [37, Sect. A].

(d) Repeat (c) for the configuration of Fig. 9.22, a case of edge radiation interference [37, Sect. B].

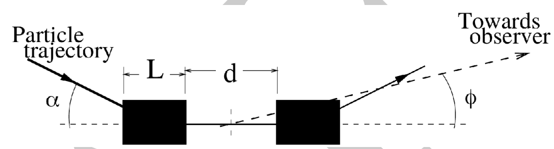

Fig. 9.22 Both dipoles have same sign. This schematic defines the observation direction $\phi = 0$

9.7 Depolarizing Resonances in SATURNE 2

Solution: page **??**

Unexpectedly as it is not a systematic resonance, $G\gamma = 7 - \nu_y$ was found to be harmful to beam polarization. Produce a crossing of that resonance, for a few particles with different momenta, and vertical invariant $\varepsilon_Z \approx 10\pi\mu$m. Take peak voltage 6 kV and synchronous phase $\phi_s = 0.2363176$ rad.

The input data file given in Tab. **??**, an outcome of exercise **??**, can be used as a starting point for this simulation.

9.8 Ion and Electron Polarization. Preservation of Polarization

More simulations regarding

- spin polarized ions and special devices and methods for the preservation of polarization during acceleration, including tune jump, partial and full Siberian snakes, etc.,

- electron spin diffusion in a storage ring and its suppression, spin matching, polarization lifetime, etc.,

can be found, with complete solutions, in the USPAS Summer 2021 Spin Class Lectures, "Polarized Beam Dynamics and Instrumentation in Particle Accelerators" [47, Chap. 14].

References

1. Christofilos, Nicholas: Focussing system for ions and electrons. US Patent Office Application filed March 10, 1950, Serial No. 148,920.
   https://patentimages.storage.googleapis.com/fa/bb/52/0ce28e28b492a6/US2736799.pdf
2. Credit: Brookhaven National Laboratory.
   https://www.flickr.com/photos/brookhavenlab/8495311598/in/album-72157611796003039/
3. Courant, Ernest D., Livingston, M. Stanley, and Snyder, Hartland S.: The Strong-Focusing Synchrotron - A New High Energy Accelerator. Phys. Rev. 88, 1190 - December 1952
4. Courant, E.D., and Snyder, H.S.: Theory of the Alternating-Gradient Synchrotron. Annals of Physics, No. 3 (1958), 1-48
5. SATURNE 2 photo: credit CEA Saclay. Archives historiques du CEA. Copyright CEA/Service de documentation
6. Credit: Lawrence Berkeley National Laboratory. The Regents of the University of California, Lawrence Berkeley National Laboratory."
7. Radial Focusing in the Linear Accelerator. Phys. Rev. Vol. 88, Num. 5, Dec. 1, 1952
8. Benedikt, M., F. Zimmermann: Status of the future circular collider study. TUYMH01 Proceedings of RuPAC2016, St. Petersburg, Russia.
   https://accelconf.web.cern.ch/rupac2016/papers/tuymh01.pdf
9. Méot, F., et al.: Progress on the optics modeling of BMI's ion rapid-cycling medical synchrotron at BNL. THPMP050, 10th Int. Particle Accelerator Conf. IPAC2019, Melbourne, Australia. https://accelconf.web.cern.ch/ipac2019/papers/thpmp050.pdf
   Copyrights under license CC-BY-3.0, https://creativecommons.org/licenses/by/3.0; no change to the material
10. Nishimori, N.: A new compact 3 GeV light source in Japan. 13th Int. Particle Acc. Conf. IPAC2022, Bangkok, Thailand.
    https://accelconf.web.cern.ch/ipac2022/papers/thixsp1.pdf
11. Méot, F.: eRHIC ERL modeling in Zgoubi. BNL-111832-2016-TECH; EIC/49;BNL-111832-2016-IR.
    https://technotes.bnl.gov/PDF?publicationId=38865
    https://www.osti.gov/biblio/1335396
12. Benabderrahmane, C.: Status of the ESRF-EBS magnets. WEPMK009, 9th International Particle Accelerator Conference, IPAC2018, Vancouver, BC, Canada.
    https://accelconf.web.cern.ch/ipac2018/papers/wepmk009.pdf
13. F. Méot, et al.: Plans For Polarized Bunch R&D at Cornell Rapid-Cycling Synchrotron. MOPMF013, 9th International Particle Accelerator Conference IPAC2018, Vancouver, BC, Canada.
    https://accelconf.web.cern.ch/ipac2018/papers/mopmf013.pdf
    Figure 9.7: Copyrights under license CC-BY-3.0, https://creativecommons.org/licenses/by/3.0; no change to the material
14. Wilson, R. R.: The 10 to 20 GeV Cornell Electron Synchrotron. Report CS-33, Laboratory of Nuclear Studies, Cornell University, Ithaca, New York (May 1, 1967)
15. D. L. Rubin, et al.: Upgrade of the Cornell electron storage ring as a synchrotron light source. WEPOB36, Proceedings of NAPAC2016, Chicago, IL, USA.
    https://accelconf.web.cern.ch/napac2016/papers/wepob36.pdf
16. CERN Courrier: Partnership yields big wins for the EIC. 27 September 2021 issue.
    https://cerncourier.com/a/partnership-yields-big-wins-for-the-eic/
17. https://www.bnl.gov/eic/
18. https://www.slac.stanford.edu/gen/grad/GradHandbook/slac.html
19. https://www.desy.de/ teslatdr/tdr_web/pages/latest_version.html
20. https://www-project.slac.stanford.edu/lc/
21. https://muoncollider.web.cern.ch/node/25
22. https://linearcollider.org/

23. Vladimir N. Litvinenko, Nikhil Bachhawat, Maria Chamizo-Llatas, Yichao Jing, François Méot, Irina Petrushina, Thomas Roser: The ReLiC: Recycling Linear e+e- Collider. arXiv:2203.06476]hep-ex]. https://doi.org/10.48550/arXiv.2203.06476
24. Jackson, G., Editor: Fermilab recycler ring technical design report. Rev. 1.1. FERMILAB-TM-1981 (July 1996). http://inspirehep.net/record/424541/files/fermilab-tm-1981.PDF
25. Méot, F.: On the Effects of Fringe Fields in the Recycler Ring. FERMILAB-TM-2016 (Aug. 1997). http://inspirehep.net/record/448603/files/fermilab-tm-2016.PDF
26. Leleux, G.: Compléments sur la Physique des Accélérateurs. DEA “Physique et Technologie des Grands Instruments”, Université Paris VI. Rapport interne LNS//86-101, CEA Saclay (1986)
27. F. Méot, et al.: Beam dynamics validation of the Halbach Technology FFAG Cell for Cornell-BNL Energy Recovery Linac. Nuclear Inst. and Methods in Physics Research, A 896 (2018) 60-67
28. Bruck, Henri: Accélérateurs circulaires de particules. Presses Universitaires de France (1966)
29. Leleux, G.: Accélérateurs Circulaires. INSTN lectures, internal report CEA Saclay (1978), unpublished
30. King, B.J.: Further studies on the prospects for many-TeV muon colliders. Procs. PAC 2001 Accel. Conf, 18-22 Jun 2001, Chicago, IL, USA. https://accelconf.web.cern.ch/p01/PAPERS/RPPH314.PDF
31. Hofmann, A.: The Physics of Synchrotron Radiation. Cambridge Monographs on Particle Physics, Nuclear Physics and Cosmology (20), Cambridge University Press (2004).
32. Leleux, G.: Rayonnement synchrotron (Aspect machine). Note technique, Laboratoire National SATURNE, CEA Saclay ,1993 (unpublished)
33. Hofmann, A. and Méot, F.: Optical resolution of beam cross-section measurements by means of synchrotron radiation. Nuclear Instruments and Methods 203 (1982) 483-493
34. Bossart, R., et al.: Proton beam profile measurements with synchrotron light. CERN-SPS-80-8-ABM, 18 June 1980
35. Méot, F: Mesure de profil par rayonnement ondulateur des faisceaux de protons et antiprotons. PhD Thesis. Report CERN/SPS 81-21 (ABM) 30 octobre 1981
36. Ponce, L., Jung, R., Méot, F.: LHC proton beam diagnostics using synchrotron radiation. Yellow Report CERN-2004-007
37. Méot, F., Ponce, L., Ponthieu, N.: Low frequency interference between short SR sources. PRST-AB, Vol. 4, 062801 (2001)
38. Méot, F.: A theory of low frequency far-field synchrotron radiation Particle Accelerators, Vol. 62, pp 215-239 (1999)
39. Méot, F.: Synchrotron radiation interferences at the LEP miniwiggler, CERN SL/94-22 (AP) (1994)
40. Méot, F.: Polarized Beam Dynamics and Instrumentation in Particle Accelerators, USPAS Summer 2021 Spin Class Lectures, Springer Nature, Open Access (2023). https://link.springer.com/book/10.1007/978-3-031-16715-7
41. Lee, S.Y: Spin Dynamics and Snakes in Synchrotrons. World Scientific (1997)
42. The 20 Years of the Synchrotron SATURNE-2. In: Proceedings of the Colloquium, Paris, France, 04 - 05 May 1998, A. Boudard and P.-A. Chamouard Editors. Edited By CEA - Laboratoire National SATURNE & CEN Saclay, France. https://doi.org/10.1142/3965
43. Plus d’anneaux autour de SATURNE (pp. 33-34) Published in: Courrier CERN Volume 39, Num. 2, Mars 1999. https://cds.cern.ch/record/1740121
44. E. Grorud, J.L. Laclare and G. Leleux: Crossing of Depolarization Resonances in Strongly Modulated Structures. IEEE Transactions on NuclearScience,Vol. NS-26,NO. 3, June 1979. https://accelconf.web.cern.ch/p79/PDF/PAC1979_3209.PDF

45. Aknin, J.P., et al.: Status report on rejuvenating SATURNE and future aspects. PAC 1979 Conference. IEEE Tans. Nucl. Sci., Vol. NS 26, No. 3, June 1979.
https://accelconf.web.cern.ch/p79/PDF/PAC1979_3138.PDF
46. Méot, F.: Polarized e-bunch acceleration at Cornell RCS: Tentative tracking simulations. Tech. Note BNL-114452-2017-TECHEIC/57;BNL-114452-2017-IR (2017).
https://technotes.bnl.gov/PDF?publicationId=42654
https://www.osti.gov/biblio/1408712
47. USPAS Summer 2021 Spin Class Lectures, "Polarized Beam Dynamics and Instrumentation in Particle Accelerators". François Méot, et al., Editors. Springer, Particle Acceleration and Detection, 2022.
https://doi.org/10.1007/978-3-031-16715-7
48. Méot, F.: Simulation of radiation damping in rings, using stepwise ray-tracing methods. 2015 JINST 10 T06006.
http://iopscience.iop.org/1748-0221/10/06/T06006
49. Gnuplot scripts to plot optical functions, reading from zgoubi.TWISS.out, can be found at
https://sourceforge.net/p/zgoubi/code/HEAD/tree/trunk/toolbox/gnuplotFiles/gnuplot_TWISS/
50. Méot, F.: Zgoubi Users' Guide. https://www.osti.gov/biblio/1062013-zgoubi-users-guide.
Sourceforge latest version: https://sourceforge.net/p/zgoubi/code/HEAD/tree/trunk/guide/Zgoubi.pdf.
The betaFromPlt.f program is available here: https://sourceforge.net/p/zgoubi/code/HEAD/tree/trunk/toolbox/betaFromPlt/